# ６．レーザープラズマ加速入門

# 【夜話】

阪大産研

**Gu Yanjun**

# 目　　次

## A Brief Introduction to Laser-driven Plasma Based Particle Acceleration

# A Brief Introduction to Laser-driven Plasma Based Particle Acceleration

Laser-plasma acceleration has been attractive since the idea of laser wakefield accelerator (LWFA) was proposed in 1979 by Tajima and Dawson. One of the advanced features of plasma acceleration is that it supports large electric field reaching 100 GV/m, which makes the potential compact accelerator to be possible. Various mechanisms for electron injection control, laser pulse guiding and beam quality improving have been proposed and demonstrated in the past decades. Electron beams up to 8 GeV with the charge quantity of tens pico-Coulomb have been addressed in experiments. With the development of laser technology, multi-PW laser is available nowadays and the corresponding intensity exceeds $10^{21}$ W/cm$^2$. It results in the generation of high energy ion beams when such an intense laser pulse irradiates on a dense target. The tens-MeV proton beams accelerated by laser-plasma interactions have the unique features of short duration, high brilliance, and low emittance. This work introduces the basic physics of laser-plasma interactions and the corresponding charged particle acceleration mechanisms. Comprehensive theoretical models for both electron and ion acceleration are presented. Practical formulas of the limited acceleration length and the energy scaling laws based on the laser-plasma parameters are given. The typical numerical method, Particle-in-cell simulation, is also briefly mentioned.

# I. Introduction to Plasma Physics

Plasma is an ionized state with free electrons and ions as its main constituents, which is often referred to as the fourth state of matter. The universe is made of dark energy, dark matter, and only 1 % normal matter. Plasma is the most predominant state of the normal matter. It can be produced by further heating the gas till the thermal energy overcomes the Coulomb potential. Thus it is easy to understand that plasma mainly exists in vacuum since air decreases the temperature resulting the electrons and ions recombination to the neutral states. Many astronomical objects are partially or fully in plasma states and allow to be detected. Although the natural plasma is rare on earth, artificial plasma has significant applications in fundamental science and industries. Capacitively coupled plasma (CCP) and inductively coupled plasma (ICP) have been widely employed in the semiconductor processing. The research of Warm dense matter (WDM) encompasses ionized fluids at the confluence of condensed matter physics, plasma physics and dense liquids. The laboratory astrophysics diagnose the plasma in experiments to model the astrophysical phenomena. Not even to mention the field of hot-plasma physics which is the fundamental of controlled nuclear fusion projects. Therefore, plasma physics includes many topics and covers a wide range of temperature and density parameters. It would be too ambitious to fully discuss all of them in a short lecture. For a more comprehensive and systematic description of plasma physics, one may consult the classical textbooks by F. F. Chen [1]. It is also one of the important references for this lecture. Concerning the laser-plasma interactions discussed in the later sections, one of the best references is by P. Gibbon [2], which also includes some basic theoretical description of plasma. Here the theoretical descriptions of plasma are focused on its features in responding the electromagnetic field and the corresponding dynamics. A better understanding of these fundamental theories would be beneficial to the further study of laser-plasma interaction and charged particle acceleration.

### 1.1 Basic Plasma Parameters

Plasma is a quasi-neutral gas with both charged particles and neutral atoms, which exhibits collective behavior. To estimate the degree of ionization under the thermal equilibrium condition, one may use the Saha equation,

$$\frac{n_i}{n_a} = 2.4 \times 10^{15} \frac{T^{3/2}}{n_i} e^{-U_i/k_B T}, \tag{1}$$

where $n_i$ and $n_a$ are the number density of the charged ions and the neutral atoms, $T$ is the temperature, $k_B$ is the Boltzmann constant and $U_i$ is the corresponding ionization potential energy. Eq. (1) shows that the ionisation fraction at room temperature is negligible. With the rise of the temperature approaching to the ionization potential energy, $n_i$ increases dramatically until the gas is fully ionized. The degree of ionization is defined as,

$$\eta = \frac{n_i}{n_i + n_a}. \tag{2}$$

One of the main differences between plasma and neutral gas is the presence of a long-range electromagnetic force. In the case of neutral gas, the interactions are mainly dominated by the collisions between neighbouring atoms and molecules. However, the charged particle motions in plasma result not only

the collisions but also the charge separation and currents. The charge separation gives rise to an electric field, while the currents induce a magnetic field. In contrast to the molecular collisions, electromagnetic field exerts a long-range influence on charged particles. Collective behavior of plasma indicates that the plasma motion not only depends on local particles states but also on the remote conditions. In fact, in many cases of plasma physics including the laser-plasma acceleration in this lecture, the long-range electromagnetic force is much larger than the local collisions so that the latter one becomes negligible. Such the plasma is called as collisionless plasma.

The collective motion of the charged particles enables plasma to respond rapidly to an external electric field. One may expect that the free electrons in plasma rearrange themselves in the vicinity of the source of the external electric field, forming a layer to screen the field as illustrated in Fig. 1(a). An anode, serving as the source of the electric field, is introduced into the plasma, resulting in the formation of an electron cloud (also called as a sheath) around the anode.

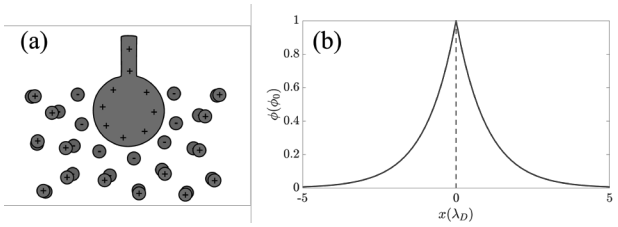


FIG. 1: (a) Schematics of Debye shielding. (b) Electric potential with respect to the Debye length.

To calculate the thickness of the electron cloud, it is non-trivial to assume that the ions are not disturbed due to the large mass. One dimensional Poisson's equation is,

$$\frac{d^2\phi}{dx^2} = -4\pi e(Zn_i - n_e) = -4\pi e(n_i - n_e), \qquad (3)$$

where $n_e$ is the electron density, e is the elementary charge, and the charge number is chosen to be $Z = 1$ for simplicity. Considering the potential energy of $-e\phi$, the electron velocity distribution function becomes:

$$f(u) = A\exp[-(\frac{1}{2}m_e u^2 - e\phi)/k_B T_e], \qquad (4)$$

where $m_e$ is the electron mass and $T_e$ is the electron temperature. Integrating over Eq. (4) as $n_e = \int_{-\infty}^{+\infty} f(u)du$ and considering the boundary conditions at infinity ($\phi \sim 0$ and $n_e = n_0$) yields the following electron density expression,

$$n_e = n_0\exp(e\phi/k_B T_e). \qquad (5)$$

Substituting $n_i$ and $n_e$ in Eq. (3) with $n_i = n_0$ and Eq. (5), one obtains

$$\frac{d^2\phi}{dx^2} = 4\pi e n_0\{[\exp(\frac{e\phi}{k_B T_e})] - 1\}. \qquad (6)$$

A Taylor expansion of the above equation, with the exclusion of the higher-order terms, yields the following equation,

$$\frac{d^2\phi}{dx^2} = \frac{4\pi n_0 e^2}{k_B T_e}\phi. \qquad (7)$$

It is now easy to get the solution of the potential distribution as

$$\phi = \phi_0\exp(-|x|/\lambda_D), \qquad (8)$$

which describes the rapid drop of the electric potential due to the plasma shielding effect, as shown in Fig. 1(b). In particular, an important parameter in plasma physics for measuring the thickness of the sheath is defined here

$$\lambda_D = \sqrt{\frac{k_B T_e}{4\pi n_0 e^2}}, \qquad (9)$$

which is called **Debye length**. Considering a system with a sufficiently large characteristic scale length ($L >> \lambda_D$), any electric potential from an external source or unbalanced charge distribution will be shielded within a short distance compared to the system size. The plasma is still globally a quasi-neutral gas.

Therefore, one of the criteria of plasma is that the ionized gas has sufficient density to make its Debye length much shorter than its size. To ensure statistical validity, it is necessary that there are sufficient particles present in the sheath,

$$N_D = \frac{4}{3}\pi\lambda_D^3 n_0 >> 1. \qquad (10)$$

The corresponding volume is called as the '**Debye sphere**'. The plasma that satisfies the condition expressed in Eq. (10) exhibits collective behavior.

### 1.2 Kinetic Theory of Plasmas

This section will introduce the kinetic theory of plasmas, with a particular focus on the collisionless Vlasov theory. Considering a system contains

a large number of particles and each of them is characterised by its charge, mass, position and velocity, i.e., $f(x_i, v_i, q_i, m_i)$. A certain particle in the position and velocity phase space (6-D) can be described as,

$$N_i(\vec{x}, \vec{v}, t) = \delta(\vec{x} - \vec{X}_i(t))\delta(\vec{v} - \vec{V}_i(t)), \tag{11}$$

which is called as the density function of single particle. At any given time, integration of the density function over the entire phase space yields the total number of particles in the system. Assuming there are two species of particles in the system, namely electrons and ions, each with $N_0$ particles. Consequently, the density of species $s$ is as follows:

$$N_s(\vec{x}, \vec{v}, t) = \sum_{i=1}^{N_0} \delta(\vec{x} - \vec{X}_i(t))\delta(\vec{v} - \vec{V}_i(t)), \tag{12}$$

and the total number of particles in the system is simply the summation of the species,

$$N_t(\vec{x}, \vec{v}, t) = \sum_{s=e,i} N_s(\vec{x}, \vec{v}, t). \tag{13}$$

The motion equation for particle $i$ is given by

$$m_s \dot{\vec{V}}_i(t) = q_s \vec{E}^m[\vec{X}_i(t), t] + \frac{q_s}{c}\vec{V}_i \times \vec{B}^m[\vec{X}_i(t), t], \tag{14}$$

which incorporates the Lorentz force. An exact equation for the evolution of a plasma can be obtained by taking the time derivative of the density functional $N_s$ in Eq. (12), which returns:

$$\begin{aligned}\frac{\partial N_s(\vec{x}, \vec{v}, t)}{\partial t} =& \sum_{i=1}^{N_0} \frac{\partial}{\partial \vec{X}_i}[\delta(\vec{x} - \vec{X}_i(t))\delta(\vec{v} - \vec{V}_i(t))]\frac{\partial \vec{X}_i}{\partial t} \\ &+ \sum_{i=1}^{N_0} \frac{\partial}{\partial \vec{V}_i}[\delta(\vec{x} - \vec{X}_i(t))\delta(\vec{v} - \vec{V}_i(t))]\frac{\partial \vec{V}_i}{\partial t}.\end{aligned} \tag{15}$$

By employing the relation of $\frac{\partial}{\partial a} f(a-b) = -\frac{\partial}{\partial b} f(a-b)$ and $\partial \vec{X}_i / \partial t = \vec{V}_i$, the above equation can be rewritten as follows:

$$\begin{aligned}\frac{\partial N_s(\vec{x}, \vec{v}, t)}{\partial t} =& -\sum_{i=1}^{N_0} \frac{\partial}{\partial \vec{x}}[\delta(\vec{x} - \vec{X}_i(t))\delta(\vec{v} - \vec{V}_i(t))]\vec{V}_i \\ &- \sum_{i=1}^{N_0} \frac{\partial}{\partial \vec{v}}[\delta(\vec{x} - \vec{X}_i(t))\delta(\vec{v} - \vec{V}_i(t))]\frac{\partial \vec{V}_i}{\partial t}.\end{aligned} \tag{16}$$

The substitution of Eq. (14) for the term $\partial \vec{V}_i / \partial t$ in Eq. (16) yields the following result:

$$\begin{aligned}\frac{\partial N_s(\vec{x}, \vec{v}, t)}{\partial t} =& -\sum_{i=1}^{N_0} \frac{\partial}{\partial \vec{x}}[\delta(\vec{x} - \vec{X}_i(t))\delta(\vec{v} - \vec{V}_i(t))]\vec{V}_i \\ &- \sum_{i=1}^{N_0} \frac{\partial}{\partial \vec{v}}[\delta(\vec{x} - \vec{X}_i(t))\delta(\vec{v} - \vec{V}_i(t))]\frac{q_s}{m_s}(\vec{E}^m + \frac{\vec{V}_i \times \vec{B}^m}{c}).\end{aligned} \tag{17}$$

According to the property of the delta function, $a\delta(a-b) = b\delta(a-b)$, the above equation transits from a specified particle to the general particles as follows:

$$\begin{aligned}\frac{\partial N_s(\vec{x}, \vec{v}, t)}{\partial t} =& -\sum_{i=1}^{N_0} \frac{\partial}{\partial \vec{x}}[\delta(\vec{x} - \vec{X}_i(t))\delta(\vec{v} - \vec{V}_i(t))]\vec{v} \\ &- \sum_{i=1}^{N_0} \frac{\partial}{\partial \vec{v}}[\delta(\vec{x} - \vec{X}_i(t))\delta(\vec{v} - \vec{V}_i(t))]\frac{q_s}{m_s}(\vec{E}^m + \frac{\vec{v} \times \vec{B}^m}{c}).\end{aligned} \tag{18}$$

It can be further simplified to the following form:

$$\frac{\partial N_s}{\partial t} + \vec{v} \cdot \frac{\partial N_s}{\partial \vec{x}} + \frac{q_s}{m_s}(\vec{E}^m + \frac{\vec{v} \times \vec{B}^m}{c})\frac{\partial N_s}{\partial \vec{v}} = 0, \tag{19}$$

which is the so called **Klimontovichi equation**. It asserts that the phase-space volume ($N_0 = \int N_s d\vec{X} d\vec{V}$) remains constant throughout the system motion along the trajectory in the phase-space. Eq. (19) is equivalent to the **Liouville's theorem** in Hamiltonian mechanics, which states that the phase volume of a Hamiltonian system in conjugate phase space is incompressible.

The Klimontovichi equation is practically unsolvable, as it is equivalent to solving the motion of all particles. Furthermore, the data is excessively detailed and may be superfluous in properly describing plasma evolution at the specified spatial and temporal scales. In comparison to the $N_s$, it is more practical to consider the smooth and continuous function by counting the number of particles of species s in the box at time $t$ with positions in the range $x$ to $x + \Delta x$ and with velocities from $v$ to $v + \Delta v$,

$$f_s(\vec{x}, \vec{v}, t) = < N_s(\vec{X}, \vec{V}, t) > = \frac{\int \int_{\Delta\Omega} N_s(\vec{X}, \vec{V}, t) d\Omega}{\Delta\Omega}, \tag{20}$$

in which $\Delta\Omega = \Delta X \Delta V$. This operation is equivalent to the transition from a series of discrete functions to a continuous function. It is possible rewrite the exact distribution functions and fields in terms of averaged ones with the fluctuations,

$$\begin{cases} N_s(\vec{X}, \vec{V}, t) = f_s(\vec{x}, \vec{v}, t) + \delta N_s(\vec{X}, \vec{V}, t) \\ \vec{E}^m(\vec{X}, \vec{V}, t) = \vec{E}(\vec{x}, \vec{v}, t) + \delta\vec{E}(\vec{X}, \vec{V}, t), \\ \vec{B}^m(\vec{X}, \vec{V}, t) = \vec{B}(\vec{x}, \vec{v}, t) + \delta\vec{B}(\vec{X}, \vec{V}, t) \end{cases} \tag{21}$$

where $\vec{E} =< \vec{E}^m >$, $\vec{B} =< \vec{B}^m >$, and $< \delta N_s >= 0$, $< \delta\vec{E} >=< \delta\vec{B} >= 0$. Substitution of the above relations into the Klimontovichi equation, Eq. (19), results in the **Plasma Kinetic equation**,

$$\frac{\partial f_s}{\partial t} + \vec{v}\cdot\frac{\partial f_s}{\partial \vec{x}} + \frac{q_s}{m_s}(\vec{E} + \frac{\vec{v}\times\vec{B}}{c})\frac{\partial f_s}{\partial \vec{v}} = -\frac{q_s}{m_s} < (\delta\vec{E} + \frac{\vec{V}\times\delta\vec{B}}{c})\frac{\partial \delta N_s}{\partial \vec{V}} > . \quad (22)$$

It is evident that the left-hand side (LHS) of the equation varies smoothly, whereas the right-hand side (RHS) represents the ensemble average of the very spiky quantities. The RHS is highly dependent on the discrete particle nature of the plasma, which gives rise to the collisions. Consequently, it can be postulated that the LHS represents collective effects, while the RHS represents the collisional effects. Expressing the collisional effect from the RHS of Eq. (22) as $(\partial f/\partial t)_c$, the **Boltzmann equation** is thus obtained as

$$\frac{\partial f_s}{\partial t} + \vec{v}\cdot\nabla_x f_s + \frac{q_s}{m_s}(\vec{E} + \frac{\vec{v}\times\vec{B}}{c})\cdot\nabla_v f_s = (\frac{\partial f}{\partial t})_c. \quad (23)$$

As previously stated in the introduction section, the collisional effects are not significant in many cases of plasma physics, which is otherwise known as the so called **collisionless plasma**. By neglecting the collisional terms on the RHS of Eq. (23), i.e. $(\partial f/\partial t)_c = 0$, one arrives at the **collisionless Boltzmann equation**,

$$\frac{\partial f_s}{\partial t} + \vec{v}\cdot\nabla_x f_s + \frac{q_s}{m_s}(\vec{E} + \frac{\vec{v}\times\vec{B}}{c})\cdot\nabla_v f_s = 0, \quad (24)$$

which is also called as the **Vlasov equation**. In general, a plasma with a high degree of ionization and a high temperature is regarded as collisionless. Nevertheless, in the case of a low-temperature plasma with weak ionization, the collisional effect cannot be neglected, and the collisionless assumption is no longer valid.

### 1.3 Fluid Description of Plasmas

In fluid mechanics, it is common to consider the motion of fluid elements rather than tracking the individual particle. The fluid equations can be derived from the moments of the Boltzmann equation. The definition of the $n^{th}$ moment for an arbitrary function $\psi(\vec{v})$ is given by

$$M_n = \int \psi(\vec{v^n}) f_s(\vec{x},\vec{v},t)d\vec{v}. \quad (25)$$

For the zeroth-order moment, one may take $\psi(\vec{v}) = 1$, which is obviously referring to the number density

$$n(\vec{x},\vec{v},t) = \int f_s(\vec{x},\vec{v},t)d\vec{v}. \quad (26)$$

It is also possible to take $\psi(\vec{v}) = m$, which is corresponding to the mass density

$$\rho(\vec{x},\vec{v},t) = \int m f_s(\vec{x},\vec{v},t)d\vec{v}. \quad (27)$$

For the first-order moment, we take $\psi(\vec{v}) = \vec{v}$ and the **drift velocity** is obtained

$$n\vec{u} = n < \vec{v} >= \int \vec{v} f_s(\vec{x},\vec{v},t)d\vec{v}. \quad (28)$$

Here we could discuss more by introducing the velocity of

$$\vec{w}(\vec{x},\vec{v},t) = \vec{v}(\vec{x},\vec{v},t) - \vec{u}(\vec{x},\vec{v},t), \quad (29)$$

which means the difference of each particle's velocity from the drift velocity. Such the velocity can also be understood as the random **thermal velocity**, which will be used later. From Eqs. (28) and (29), it is easy to know that $< w >= 0$, i.e., the random thermal velocity has a mean value of 0.

For the second-order moment, we take $\psi(\vec{v}) = m\vec{v}\vec{v}$, where $\vec{v}\vec{v}$ is a tensor containing 9 components,

$$\vec{v}\vec{v} = \begin{bmatrix} v_1v_1 & v_1v_2 & v_1v_3 \\ v_2v_1 & v_2v_2 & v_2v_3 \\ v_3v_1 & v_3v_2 & v_3v_3 \end{bmatrix} \quad (30)$$

Then the Second-order moment becomes

$$nm < \vec{v}\vec{v} >= \int m\vec{v}\vec{v} f_s(\vec{x},\vec{v},t)d\vec{v}. \quad (31)$$

Recalling the thermal velocity in Eq. (29), the second-order moment can be rewritten as

$$\begin{aligned} nm < \vec{v}\vec{v} >&= nm < (\vec{u}+\vec{w})(\vec{u}+\vec{w}) > \\ &= nm < \vec{u}\vec{u} + \vec{u}\vec{w} + \vec{w}\vec{u} + \vec{w}\vec{w} > \\ &= nm\vec{u}\vec{u} + nm < \vec{w}\vec{w} >, \end{aligned} \quad (32)$$

in which the truth of $< \vec{w} >= 0$ is used. The second term on the RHS of Eq. (32) is the **Total pressure tensor**. It can be further factorized as

$$\overleftrightarrow{p} = p\overleftrightarrow{I} + \overleftrightarrow{\pi}, \quad (33)$$

in which

$$\overleftrightarrow{pI} = nm \begin{bmatrix} w_1w_1 & 0 & 0 \\ 0 & w_2w_2 & 0 \\ 0 & 0 & w_3w_3 \end{bmatrix} \tag{34}$$

is the **Pressure Tensor** and

$$\overleftrightarrow{\Pi} = nm \begin{bmatrix} 0 & w_1w_2 & w_1w_3 \\ w_2w_1 & 0 & w_2w_3 \\ w_3w_1 & w_3w_2 & 0 \end{bmatrix} \tag{35}$$

is the **Viscous Stress Tensor**.

Based on the previous derivations, now we may take the velocity moment $\psi(\vec{v})$ for the Boltzmann equation (23) as the following form in Eq. (36) in order to obtain the fluid descriptions of plasma.

$$\int \psi(\vec{v})[\frac{\partial f_s}{\partial t} + \vec{v}\cdot\nabla_x f_s + \frac{q_s}{m_s}(\vec{E} + \frac{\vec{v}\times\vec{B}}{c})\cdot\nabla_v f_s]d\vec{v} = \int \psi(\vec{v})(\frac{\partial f}{\partial t})_c d\vec{v}. \tag{36}$$

The first term on the LHS can be expressed as

$$\int \psi(\vec{v})\frac{\partial f_s}{\partial t}d\vec{v} = \frac{\partial}{\partial t}\int \psi(\vec{v})f_s d\vec{v} = \frac{\partial}{\partial t}(n < \psi(\vec{v}) >), \tag{37}$$

where the relation of $< nx >= \int x f_s d\vec{v}$ is employed. The second term on the LHS can be obtained similarly

$$\int \psi(\vec{v})\vec{v}\cdot\nabla_x f_s d\vec{v} = \nabla_x \int \psi(\vec{v})\vec{v}\cdot f_s d\vec{v} = \nabla_x\cdot(n < \psi(\vec{v})\vec{v} >) \tag{38}$$

The third term is a little bit complicate and it's better to calculate the electric part and magnetic part separately. The electric component part is

$$\frac{q_s\vec{E}}{m_s}\int \psi(\vec{v})\nabla_v f_s d\vec{v} = \frac{q_s\vec{E}}{m_s}[f_s\psi(\vec{v})\Big|_c - \int f_s\nabla_v\psi(\vec{v})] = -\frac{nq_s\vec{E}}{m_s} < \nabla_v\psi(\vec{v}) >, \tag{39}$$

in which the integration by parts method is used. The magnetic component part can be operated similarly,

$$\begin{aligned} &\frac{q_s}{m_s c}\int \psi(\vec{v})(\vec{v}\times\vec{B})\cdot\nabla_v f_s d\vec{v} \\ &= \frac{q_s}{m_s c}[f_s(\vec{v}\times\vec{B})\psi(\vec{v})\Big|_c - \int f_s\nabla_v(\psi(\vec{v})(\vec{v}\times\vec{B}))d\vec{v}] \\ &= -\frac{nq_s}{m_s c} < (\vec{v}\times\vec{B})\nabla_v\psi(\vec{v}) > . \end{aligned} \tag{40}$$

In conclusion, the velocity moment in Eq. (36) has the form of

$$\begin{aligned} &\frac{\partial}{\partial t}(n < \psi(\vec{v}) >) + \nabla_x\cdot(n < \psi(\vec{v})\vec{v} >) \\ &- \frac{nq_s}{m_s}(\vec{E} + \frac{< \vec{v}\times\vec{B} >}{c}) < \nabla_v\psi(\vec{v}) >= \int \psi(\vec{v})(\frac{\partial f}{\partial t})_c d\vec{v}. \end{aligned} \tag{41}$$

This is the general form of the velocity moment $\psi(\vec{v})$ for the Boltzmann equation. A series of conservation equations can be derived from Eq. (41).

Considering the zeroth-order, we may take $\psi(\vec{v}) = 1$ and plug it into Eq. (41) and derive that

$$\frac{\partial n}{\partial t} + \nabla_x\cdot(n\vec{u}) = 0, \tag{42}$$

which is the so-called **Continuity equation**. It is also possible to take $\psi(\vec{v}) = m$ and derives

$$\frac{\partial \rho}{\partial t} + \nabla_x\cdot(\rho\vec{u}) = 0, \tag{43}$$

which is the **MHD Mass Conservation equation**.

For the first-order, it is $\psi(\vec{v}) = m\vec{v}$ similar to the previous section,

$$\frac{\partial nm\vec{u}}{\partial t} + \nabla_x\cdot(nm < \vec{v}\vec{v} >) - nq(\vec{E} + \frac{\vec{u}\times\vec{B}}{c}) = \vec{R}, \tag{44}$$

where $\vec{R}$ is the frictional force density. Recalling the relation in Eqs. (32) and (33), we have $nm < \vec{v}\vec{v} >= nm(\vec{u}\vec{u}) + p\overleftrightarrow{I} + \overleftrightarrow{\Pi}$. Eq. (44) can therefore be rewritten as

$$\frac{\partial(nm\vec{u})}{\partial t} + \nabla_x\cdot(nm\vec{u}\vec{u}) = nq(\vec{E} + \frac{\vec{u}\times\vec{B}}{c}) - \nabla_x p - \nabla_x\cdot\overleftrightarrow{\Pi} + \vec{R}, \tag{45}$$

which is called **MHD Momentum Equation**. Furthermore, by introducing the **advective derivative** or **Lagrange derivative** as

$$\frac{D}{Dt} = \frac{\partial}{\partial t} + \vec{u}\cdot\nabla_x, \tag{46}$$

a more general form of Eq. (45) can be derived as

$$mn\frac{D\vec{u}}{Dt} = nq(\vec{E} + \frac{\vec{u}\times\vec{B}}{c}) - \nabla_x p - \nabla_x\cdot\overleftrightarrow{\Pi} + \vec{R}. \tag{47}$$

In Eq. (47), the RHS terms have clearly physical meaning which represent the Lorentz force, thermal pressure, viscosity and friction, respectively.

For the second-order, we take $\psi(\vec{v}) = m\vec{v^2}/2$ and then the **Energy Conservation equation** can be derived,

$$\frac{\partial K}{\partial t} = -\nabla\cdot\vec{q} + qn\vec{u}\cdot\vec{E} + \vec{u}\cdot\vec{R} + Q, \tag{48}$$

where $K =< nmv^2/2 >$ is the kinetic energy density, $\vec{q} = n < \vec{v}mv^2/2 >$ is the conductive heat flux. The last two terms are contributed by the elastic collisions as

$$\int \frac{1}{2}mv^2(\frac{\partial f}{\partial \vec{v}})_c d\vec{v} = \frac{m}{2}\int (u^2 + 2\vec{u}\vec{w} + w^2)(\frac{\partial f}{\partial \vec{v}})_c d\vec{v} = \vec{u}\cdot\vec{R} + Q. \tag{49}$$

Here $\vec{R}$ is the frictional force density and $Q$ is the energy exchange density. Basically, Eq. (48) describes the mechanism of the energy evolution and the terms on the RHS indicate the work done by pressure, the Joule heating, frictional heating and the collision effect. By applying the continuity equation and the MHD momentum equation, the energy conservation equation will have the simplified form as

$$\frac{3}{2}n\frac{dT}{dt} = -(\overleftrightarrow{p}\cdot\nabla)\cdot\vec{u} - \nabla\cdot\vec{q} + Q, \tag{50}$$

which is also called as the **Thermal equilibrium equation**. The RHS terms represent viscosity, thermal conduction and the heat exchange from collisions.

The continuity equation (42), the MHD momentum equation (45) and the energy Conservation equation (50) establish the plasma **Two-fluid equations**.

$$\begin{cases} \frac{\partial n_\alpha}{\partial t} + \nabla_x\cdot(n_\alpha\vec{u}_\alpha) = 0, \\ m_\alpha n_\alpha \frac{D\vec{u}_\alpha}{Dt} = n_\alpha q_\alpha(\vec{E} + \frac{\vec{u}_\alpha\times\vec{B}}{c}) - \nabla_x p_\alpha - \nabla_x\cdot\overleftrightarrow{\Pi}_\alpha + \vec{R}_\alpha, \\ \frac{3}{2}n_\alpha\frac{dT_\alpha}{dt} = -(\overleftrightarrow{p}_\alpha\cdot\nabla)\cdot\vec{u}_\alpha - \nabla\cdot\vec{q}_\alpha + Q_\alpha, \end{cases} \tag{51}$$

where $\alpha = e, i$ refers to the electrons and ions. Together with **Maxwell's equations** in (52), the full fluid description of plasmas are established.

$$\begin{cases} \nabla\cdot\vec{E} = 4\pi en, \\ \nabla\times\vec{E} = -\frac{1}{c}\frac{\partial\vec{B}}{\partial t}, \\ \nabla\cdot\vec{B} = 0, \\ \nabla\times\vec{B} = \frac{4\pi}{c}\vec{j} + \frac{1}{c}\frac{\partial\vec{E}}{\partial t}, \\ \vec{j} = ne\vec{u}. \end{cases} \tag{52}$$

### 1.4 Closure Problem

It is evident that the Two-fluid equations (51) are not closure. The $n^{th}$ order moment equation always involves the $(n+1)^{th}$ order moment of the distribution function. This hierarchy occurs because the $\vec{v}\cdot\nabla_x f_s$ term in the Boltzmann equation always increases the order of the moments by one. This is called the **Closure Problem**. Therefore to obtain a closed set of equations it is then necessary to cut-off the $(n+1)^{th}$ order moment by assuming some equations of state. For example, in a sufficiently collisional plasma that is in thermodynamic equilibrium, we may use the well-known thermodynamics equations to describe the plasma state. In a collisionless plasma, however, this approach often fails. Some of the most commonly used equations of state are discussed here.

The first is the cold plasma state. In this case, we assume that the temperature of the plasma is zero ($T_e = 0$) and the corresponding pressure tensor is also zero ($\overleftrightarrow{p} = p\overleftrightarrow{I} = \overleftrightarrow{\Pi} = 0$). Therefore the fluid equations are simplified to

$$\begin{cases} \frac{\partial n_\alpha}{\partial t} + \nabla_x\cdot(n_\alpha\vec{u}_\alpha) = 0, \\ m_\alpha n_\alpha\frac{D\vec{u}_\alpha}{Dt} = n_\alpha q_\alpha(\vec{E} + \frac{\vec{u}_\alpha\times\vec{B}}{c}), \end{cases} \tag{53}$$

which is the equations of the cold plasma.

The second is the adiabatic state. Such the concept is borrowed from the thermodynamics. Consider the ideal gas state and the first law of thermodynamics,

$$\begin{cases} pV = nk_BT, \\ dQ = dU + pdV. \end{cases} \tag{54}$$

In the adiabatic case, it assumes that $dQ = 0$ and the corresponding equation of state can be derived as

$$pV^\gamma = const, \tag{55}$$

in which $\gamma = f + 2/f$ based on statistical physics and $f$ is the freedom degrees of the gas.

### 1.5 Waves in Plasmas

Waves in plasmas are an interconnected set of particles and fields that propagate periodically. The motion of ions is much slower than that of electrons due to their heavier mass. Therefore, in many cases with a relatively short time scale, we can consider the ions as a static background and focus only on the electron waves. Now we apply a perturbation theory to the above situations by assuming that

$$\begin{cases} n_e = n_0 + \tilde{n}_e, \\ \vec{u}_e = \vec{u}_0 + \tilde{u} = \tilde{u}, \\ \vec{E} = \vec{E}_0 + \tilde{E}, \end{cases} \tag{56}$$

in which the $n_e$, $\vec{u}_0$ and $\vec{E}_0$ are the steady quantity with the property of $\partial n_e/\partial t = \vec{E}_0 = \vec{u}_0 = 0$. We also assume that the plasma is non-magnetized and there is no external magnetic field ($\vec{B} = 0$).The assumption of cold plasmas means that the temperature of the plasma is zero ($T_e = 0$) and the corresponding pressure tensor is also zero ($\overleftrightarrow{p} = p\overleftrightarrow{I} = \overleftrightarrow{\Pi} = 0$).

In this case the plasma state can be further simplified according to Eq. (53) and Maxwell's equations (52),

$$\begin{cases} \frac{\partial n_e}{\partial t} + \nabla_x \cdot (n_e \vec{u_e}) = 0, \\ m_e n_e \frac{\partial \vec{u_e}}{\partial t} + m_e n_e (\vec{u_e} \cdot \nabla) \vec{u_e} = -n_e e \vec{E}, \\ \nabla \cdot \vec{E} = 4\pi e (n_{i0} - n_e). \end{cases} \tag{57}$$

Substituting Eq. (56) into Eq. (57) and ignoring the second-order infinitesimal, e.g. $(\tilde{n}\tilde{u})$ and $(\tilde{u}\nabla\tilde{u})$, the above equations can be linearized

$$\begin{cases} \frac{\partial \tilde{n}}{\partial t} + \nabla_x \cdot (n_0 \tilde{u}) = 0, \\ m_e n_e \frac{\partial \tilde{u}}{\partial t} = -n_0 e \tilde{E}, \\ \nabla \cdot \tilde{E} = -4\pi e \tilde{n}. \end{cases} \tag{58}$$

Using the relation of $\nabla \sim ik$ and $\partial/\partial t \sim -i\omega$, the above equations can be **Fourier transformed**

$$\begin{cases} -i\omega\tilde{n} + ik(n_0\tilde{u}) = 0, \\ -i\omega n_0 m_e \tilde{u} = -n_0 e \tilde{E}, \\ ik\tilde{E} = -4\pi e \tilde{n}. \end{cases} \tag{59}$$

The dispersion equation can be written as

$$\omega\tilde{n} - \frac{4\pi n_0 e^2}{\omega m_e}\tilde{n} = 0. \tag{60}$$

This gives the frequency of the plasma oscillation is obtained

$$\omega_{pe}^2 = \frac{4\pi n_0 e^2}{m_e}. \tag{61}$$

The plasma oscillation is also known as the '**cold Langmuir wave**', which is a rapid oscillation of the electron density in plasmas. However, this wave does not propagate but oscillates locally.

Different from the cold plasma condition, we now consider that the plasma has a temperature and the corresponding thermal pressure. However, the thermal velocity of the electrons is much lower than that of the wave velocity, which means that the electrons have no time for the thermal exchange during the wave propagation. In other words, the plasma is in an adiabatic state. Recall the adiabatic state in Eq. (55),

$$p_e V^\gamma = p_e n_e^{-\gamma} = const. \tag{62}$$

Do the derivative on both sides, $\nabla(p_e n_e^{-\gamma}) = \nabla(p_e) n_e^{-\gamma} - p_e \gamma n_e^{-\gamma-1} \nabla n_e = 0$, it results the pressure gradient

$$\nabla p_e = \frac{\gamma p_e}{n_e} \nabla n_e. \tag{63}$$

Given the ideal thermal equilibrium condition of $p_e = n_e k_B T_e$ and the adiabatic index $\gamma = f + 2/f = 3$, the pressure gradient term can be expressed as

$$\nabla p_e = \frac{\gamma n_e k_B T_e}{n_e} \nabla n_e = \gamma_e k_B T_e \nabla n_e. \tag{64}$$

Compared to Eq. (58), we only need to add the pressure gradient term in the Momentum equation and the total fluid equations are linearized to be

$$\begin{cases} \frac{\partial \tilde{n}}{\partial t} + \nabla_x \cdot (n_0 \tilde{u}) = 0, \\ m_e n_e \frac{\partial \tilde{u}}{\partial t} = -n_0 e \tilde{E} - \gamma_e k_B T_e \nabla \tilde{n}, \\ \nabla \cdot \tilde{E} = -4\pi e \tilde{n}. \end{cases} \tag{65}$$

The corresponding Fourier transformed equations can be expressed as

$$\begin{cases} -i\omega\tilde{n} + ik(n_0\tilde{u}) = 0, \\ -i\omega n_0 m_e \tilde{u} = -n_0 e \tilde{E} - \gamma_e i k k_B T_e \tilde{n}, \\ ik\tilde{E} = -4\pi e \tilde{n}. \end{cases} \tag{66}$$

Then the dispersion relation can be written as

$$\omega^2 = \omega_{pe}^2 + \frac{3k_B T_e}{m_e} k^2 = \omega_{pe}^2 + \gamma_e k^2 v_{th}^2, \tag{67}$$

where $v_{th} = k_B T_e / m_e$ is the electron thermal velocity. Eq. (67) is also known as the **Bohm–Gross dispersion relation**. It states that the electron pressure acts as a restoring force as well as the electric field when the electron thermal motion is taken into account. The electron plasma wave is also known as the **Lamgmuir wave**. The corresponding dispersion relation is shown in Fig. (2). Only when the frequency is higher than that of the plasma oscillation frequency ($\omega_{pe}$) can the Langmuir wave propagate.

On a longer time scale ($t \sim \omega_{pi}^{-1}$), it is non-trivial to consider the ion motion and its corresponding wave mode. However, the situation becomes much more complex and it is necessary to describe the plasmas according to the Two fluid equations (51). Nevertheless, it is possible to use some approximations to simplify the equations. First, similar to the case above, the adiabatic condition is valid. Second, the electron motions in the plasma now follow the ions. Considering $m_e << m_i$, we assume that $m_e = 0$ and the momentum of the electrons is negligible. Therefore the Two fluid equations in this case can be rewritten as,

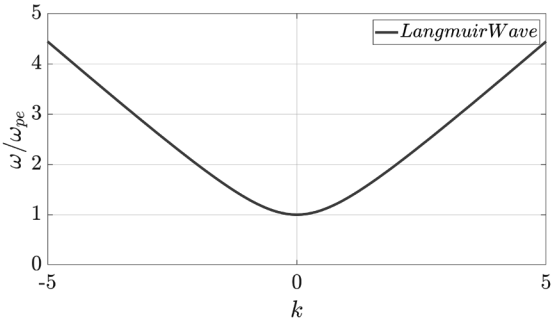


FIG. 2: The dispersion relation of the Langmuir wave.

$$\begin{cases} \frac{\partial n_e}{\partial t} + \nabla \cdot (n_e \vec{u}_e) = 0, \\ -n_e e\vec{E} - \gamma_e k_B T_e \nabla n_e = 0, \\ \frac{\partial n_i}{\partial t} + \nabla_x \cdot (n_i \vec{u}_i) = 0, \\ m_i n_i \frac{\partial \vec{u}_i}{\partial t} + m_i n_i (\vec{u}_i \cdot \nabla)\vec{u_i} = n_i e\vec{E} - \gamma_i k_B T_i \nabla n_i, \\ \nabla \cdot \vec{E} = 4\pi e(n_i - n_e). \end{cases} \tag{68}$$

Linearizing and Fourier transforming the equations with the relation of $n_e = n_0 + \tilde{n}_e$, $n_i = n_0 + \tilde{n}_i$, one obtains

$$\begin{cases} -i\omega\tilde{n}_e + ik(n_0\tilde{u}_e) = 0, \\ -n_0 e\tilde{E} - i\gamma_e k k_B T_e \tilde{n}_e = 0, \\ -i\omega\tilde{n}_i + ik(n_0\tilde{u}_i) = 0, \\ -i\omega n_0 m_i \tilde{u}_i = n_0 e\tilde{E} - i\gamma_i k k_B T_i \tilde{n}_i, \\ ik\tilde{E} = 4\pi e(\tilde{n}_i - \tilde{n}_e). \end{cases} \tag{69}$$

First consider the case of low frequency and long wavelength, where the high frequency components can be neglected as $\partial\tilde{n}_e/\partial t = \partial\tilde{u}_e/\partial t = 0$. Furthermore, in this case the perturbation of the electrons follows the perturbation of the ions, i.e. $\tilde{n}_e = \tilde{n}_i$. The plasma is quasi-neutral in the wavelength range. Thus, the above equations can be reduced to

$$\begin{cases} -n_0 e\tilde{E} - i\gamma_e k k_B T_e \tilde{n}_e = 0, \\ -i\omega\tilde{n}_i + ik(n_0\tilde{u}_i) = 0, \\ -i\omega n_0 m_i \tilde{u}_i = n_0 e\tilde{E} - i\gamma_i k k_B T_i \tilde{n}_i, \end{cases} \tag{70}$$

in the case of low frequency and long wavelength. The corresponding dispersion relation is obtained as

$$\omega^2 = \frac{k_B(\gamma_e T_e + \gamma_i T_i)}{m_i} k^2. \tag{71}$$

Since the frequency is now proportional to the wavenumber, it is very similar to the case of the sound wave, where the phase velocity is equal to the group velocity. We can therefore define the **Ion acoustic wave speed** as

$$v_s = \sqrt{\frac{k_B(\gamma_e T_e + \gamma_i T_i)}{m_i}}, \tag{72}$$

which has a form very similar to the sound speed of a neutral gas $c_s = \sqrt{\gamma p_0/\rho_0} = \sqrt{\gamma T/m}$. Thus Eq. (71) can be rewritten as $\omega^2 = v_s^2 k^2$. It is clear that $v_g = d\omega/dk = v_s$ and also $v_p = \omega/k = v_s$.

Secondly, we consider the case of low frequency but short wavelength. In this case the plasma is no longer quasi-neutral in the wavelength range and therefore $\tilde{n}_e = \tilde{n}_i$ is not valid here. Eqs. (69) now have the following form,

$$\begin{cases} -n_0 e\tilde{E} - i\gamma_e k k_B T_e \tilde{n}_e = 0, \\ -i\omega\tilde{n}_i + ik(n_0\tilde{u}_i) = 0, \\ -i\omega n_0 m_i \tilde{u}_i = n_0 e\tilde{E} - i\gamma_i k k_B T_i \tilde{n}_i, \\ ik\tilde{E} = 4\pi e(\tilde{n}_i - \tilde{n}_e). \end{cases} \tag{73}$$

The dispersion relation is obtained as

$$\omega^2 = [\frac{\gamma_i k_B T_i}{m_i} + \frac{\gamma_e k_B T_e}{m_i(1 + \gamma_e k^2 \lambda_D^2)}]k^2, \tag{74}$$

in which $\lambda_D$ is the Debye Length of the plasma according to Eq. (9). From Eq. (74), we could see that in the case of $k\lambda_D << 1$, it transits back to the form of Eq. (71). It can be summarized as

$$\begin{cases} \omega^2 = v_s^2 k^2, & v_s = \sqrt{\frac{k_B(\gamma_e T_e + \gamma_i T_i)}{m_i}}, \quad (k\lambda_D << 1) \\ \omega^2 = \omega_{pi}^2 + \gamma_i v_i^2 k^2, & v_i = \sqrt{k_B T_i} m_i, \quad (k\lambda_D >> 1). \end{cases} \tag{75}$$

In the study of laser-plasma interactions, it is important to know how the electromagnetic field propagates in the plasmas and the corresponding dispersion relation. Since the EM field is a high-frequency oscillation, therefore the ions can be regarded as immobile unless the field is strong enough to push the ions as fast as electrons. The following equations are considered,

$$\begin{cases} m_e n_e \frac{\partial \vec{u}_e}{\partial t} + m_e n_e (\vec{u}_e \cdot \nabla)\vec{u_e} = -n_e e(\vec{E} + \frac{\vec{u_e} \times \vec{B}}{c}), \\ \nabla \times \vec{E} = -\frac{1}{c}\frac{\partial \vec{B}}{\partial t}, \\ \nabla \times \vec{B} = \frac{4\pi\vec{j}}{c} + \frac{1}{c}\frac{\partial \vec{E}}{\partial t}, \\ \vec{j} = -en_e\vec{u}_e. \end{cases} \tag{76}$$

Recall the perturbation theory in Eqs. (56) again and neglect the high-order infinitesimal, the above equations can be lineraized as

$$\begin{cases} m_e n_0 \frac{\partial \tilde{u}_e}{\partial t} = -n_0 e\tilde{E}, \\ \nabla \times \tilde{E} = -\frac{1}{c}\frac{\partial \tilde{B}}{\partial t}, \\ \nabla \times \tilde{B} = \frac{4\pi\tilde{j}}{c} + \frac{1}{c}\frac{\partial \tilde{E}}{\partial t}, \\ \vec{j} = -en_0\tilde{u}_e. \end{cases} \tag{77}$$

According to the vector identities, the above equations can be rewritten as:

$$\begin{aligned}
&\nabla \times \tilde{E} = -\frac{1}{c}\frac{\partial \tilde{B}}{\partial t} \\
&\nabla \times (\nabla \times \tilde{E}) = -\frac{1}{c}\frac{\partial}{\partial t}(\nabla \times \tilde{B}) \\
&\nabla(\nabla \cdot \tilde{E}) - \nabla^2 \tilde{E} = -\frac{4\pi}{c^2}\frac{\partial \tilde{j}}{\partial t} - \frac{1}{c^2}\frac{\partial^2 \tilde{E}}{\partial t^2} \\
&\nabla^2 \tilde{E} - \frac{1}{c^2}\frac{\partial^2 \tilde{E}}{\partial t^2} = -\frac{4\pi n_0 e}{c^2}\frac{\partial \tilde{u}_e}{\partial t} \\
&\nabla^2 \tilde{E} - \frac{1}{c^2}\frac{\partial^2 \tilde{E}}{\partial t^2} = \frac{4\pi n_0 e^2}{m_e c^2}\tilde{E} \\
&c^2\nabla^2 \tilde{E} - \frac{\partial^2 \tilde{E}}{\partial t^2} = \omega_{pe}^2 \tilde{E}.
\end{aligned} \tag{78}$$

Fourier transforms the above equation, the **dispersion relation of EM field in the plasmas** is obtained,

$$\omega^2 = \omega_{pe}^2 + c^2 k^2. \tag{79}$$

According to Eq. (79), we can derive an important density parameter in the laser-plasma interactions. In order for an EM wave to propagate in the plasmas, the cut-off frequency should be $\omega \geq \omega_{pe}$. Therefore, we have the corresponding plasma density, which is called as **critical density**,

$$n_c = \frac{m_e \omega^2}{4\pi e^2}. \tag{80}$$

One of the famous applications of the critical density is the radio communications. The ionosphere is the ionized part of the upper atmosphere of the Earth, from about 48 km to 965 km above sea level, a region that includes the thermosphere and parts of the mesosphere and exosphere. The ionosphere is ionized by solar radiation. The density of the ionosphere is critical for radio waves. Therefore, instead of penetrating into space, radio waves are reflected by the ionosphere and can be received at the other end of the Earth.

# II. Electron Dynamics in EM Field

This section introduces the single electron motion in a given electromagnetic field. While the model of single electron motion does not take into account the impact of currents, it is essential to derive the electron dynamics and introduce the necessary notations before addressing the complex laser-plasma interactions. A better understanding of particle dynamics will provide insight into the basic properties of a plasma interacting with laser pulse.

Here the electric field and magnetic field are represented by the potential vector,

$$\mathbf{E} = -\frac{1}{c}\frac{\partial \mathbf{A}}{\partial t}, \tag{81}$$

$$\mathbf{B} = \nabla \times \mathbf{A}. \tag{82}$$

### 2.1 Free Electron in an EM Plane Wave

Considering the linear polarized electromagnetic field is a plane wave propagating along the $x-$direction and the electric component is oscillating in the $y-$direction. Therefore the potential vector has only the $y-$component, i.e., $\mathbf{A} = A(0, A_y, 0)$. The corresponding electric field and magnetic field can be expressed as,

$$E_y = -\frac{1}{c}\frac{\partial A_y}{\partial t}, \tag{83}$$

$$B_z = \frac{\partial A_y}{\partial x}. \tag{84}$$

The equation of motion of an electron is governed by the Lorentz force

$$\frac{d\mathbf{p}}{dt} = -e(\mathbf{E} + \frac{\mathbf{v} \times \mathbf{B}}{c}). \tag{85}$$

Dot product a velocity vector $\mathbf{v}$ on both sides of Eq. (85), i.e., $\mathbf{v} \cdot d\mathbf{p}/dt = -e\mathbf{v} \cdot (\mathbf{E} + \mathbf{v} \times \mathbf{B}/c)$, so the term on the LHS can be expressed as

$$\mathbf{v} \cdot \frac{d\mathbf{p}}{dt} = \mathbf{v} \cdot \frac{d(\gamma m_e \mathbf{v})}{dt}. \tag{86}$$

It is easy to see that Eq. (86) is actually the time derivative of the kinetic energy, i.e., $d\varepsilon/dt$. The second term on the RHS, $\mathbf{v} \cdot (\mathbf{v} \times \mathbf{B})$, is zero. Then we have the energy equation of the electron as,

$$\frac{d\varepsilon}{dt} = -e\mathbf{v} \cdot \mathbf{E}. \tag{87}$$

Eq. (87) also reveals the truth that the magnetic field does not do any work on the particles, only the electric field provides energy to the particles.

Since the electric field has only the $y-$component, the corresponding velocity in Eq. (87) can be replaced by $v_y$. Substituting the electric field by Eq. (83) gives the following equation,

$$\frac{d\varepsilon}{dt} = \frac{ev_y}{c}\frac{\partial A_y}{\partial t}. \tag{88}$$

The electron momentum can be regarded as the vector addition of its longitudinal component and transverse components, i.e., $\mathbf{p} = \mathbf{p}_\parallel + \mathbf{p}_\perp$. Here, the transverse component is considered first.

$$\frac{dp_\perp}{dt} = -e(E_y - \frac{v_x B_z}{c}). \tag{89}$$

Substituting the electric field and magnetic field by the potential vector expression in Eq. (83) and (84), the above equation varies to,

$$\frac{dp_\perp}{dt} = \frac{e}{c}(\frac{\partial A_y}{\partial t} + v_x\frac{\partial A_y}{\partial x}). \tag{90}$$

Since the $A_y$ is a function of $x$ and $t$, thus the total derivative of $A_y$ is $dA_y = (\partial A_y/\partial t)dt + (\partial A_y/\partial x)dx$. Therefore $dA_y/dt = \partial A_y/\partial t + v_x\partial A_y/\partial x$. According to Eq. (90), the conservation equation for the transverse momentum can be obtained as,

$$\frac{d}{dt}(p_\perp - \frac{e}{c}A_y) = 0. \tag{91}$$

Similarly, the longitudinal momentum equation can be expressed as,

$$\frac{dp_\parallel}{dt} = -e(\frac{v_y B_z}{c}) = -\frac{ev_y}{c}\frac{\partial A_y}{\partial x}. \tag{92}$$

Combining Eqs. (88) and (92), gives

$$\frac{d}{dt}(\varepsilon - cp_\parallel) = \frac{ev_y}{c}(\frac{\partial A_y}{\partial t} + c\frac{\partial A_y}{\partial x}). \tag{93}$$

For a plane wave propagating in the $x-$direction, the potential vector has such the form as

$$A(x,t) = A_0 e^{i(kx-\omega t)}. \tag{94}$$

In this case, the RHS term of Eq. (93) gives $\frac{\partial A_y}{\partial t} + c\frac{\partial A_y}{\partial x} = -i\omega + ck$, which is zero with the condition of $\omega = ck$. Then the conservation equation with the kinetic energy and the longitudinal momentum is obtained as,

$$\frac{d}{dt}(\varepsilon - cp_\parallel) = 0. \tag{95}$$

The electron motion trajectory can be derived from the conservation equations of transverse (Eq. (91)) and longitudinal momentum (Eq. (95)). The integration of Eq. (91) gives

$$p_\perp = \frac{e}{c}A_y + p_{\perp,0}. \tag{96}$$

Here the integration constant is chosen to be $p_{\perp,0} = 0$ and the term of $\frac{e}{m_e c^2}A_y = a_0\cos\phi$ is rewritten, where $\phi = \omega t - kx$ is the phase of the wave and $a_0$ is the dimensionless amplitude of the laser field. Then the transverse momentum can simply be expressed as,

$$\tilde{p}_\perp = a_0\cos\phi, \tag{97}$$

where $\tilde{p}_\perp = p_\perp/(m_e c)$ is the dimensionless momentum. According to Eq. (95), the integration gives

$$\varepsilon = cp_\parallel + m_e c^2. \tag{98}$$

Here the integration constant should be the rest mass energy of an electron, i.e., $\varepsilon_0 = m_e c^2$. Square both sides of the equation, one obtains

$$\varepsilon^2 = c^2 p_\parallel^2 + (m_e c^2)^2 + 2m_e c^3 p_\parallel. \tag{99}$$

Note that the square of kinetic energy can also be expressed as

$$\varepsilon^2 = c^2 p_\parallel^2 + c^2 p_\perp^2 + (m_e c^2)^2. \tag{100}$$

Comparing Eqs. (99) and (100), the terms of $(m_e c^2)^2$ and $c^2 p_\parallel^2$ can be eliminated. The relationship between the transverse and the longitudinal momentum is obtained as $p_\perp^2 = 2m_e c p_\parallel$. Using the dimensionless momentum, a more simplified relationship can be expressed as

$$\tilde{p}_\perp^2 = 2\tilde{p}_\parallel. \tag{101}$$

Recalling Eqs. (97) and (101), the momentum components are now solved as

$$\begin{cases} \tilde{p}_\parallel = \frac{a_0^2}{4}(1 + \cos 2\phi), \\ \tilde{p}_\perp = a_0\cos\phi. \end{cases} \tag{102}$$

The integration of Eq. (102) gives the trajectory of the electron. Since $\phi = \omega t - kx$, the time integration can be considered as an integration in $\phi$. Therefore, the solution is obtained

$$\begin{cases} x = \frac{a_0^2}{4}(\phi + \frac{\sin 2\phi}{2}), \\ y = a_0\sin\phi. \end{cases} \tag{103}$$

Considering the average drift velocity of an electron in a laser cycle, i.e. taking the integration from

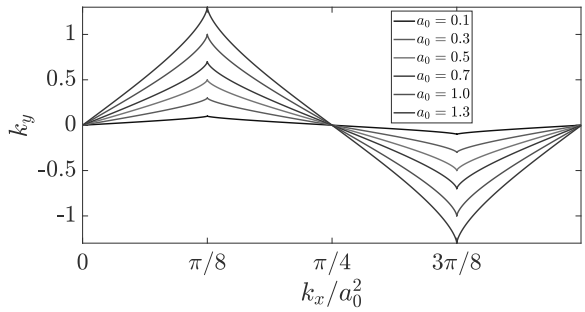


FIG. 3: Electron orbits in a plane wave.

$\phi_0 = 0$ to $\phi_t = 2\pi$. The corresponding electron orbits at different laser amplitudes are shown in Figure 3. The periodic motion in $y-$direction according to Eq. (102) gives $\tilde{p}_{\perp,t} - \tilde{p}_{\perp,0} = 0$, i.e., $< v_y >= 0$. The transverse oscillation amplitude is proportional to $a_0$.

However, in the $x-$direction, the longitudinal momentum increases to $\tilde{p}_{\parallel,t} = a_0^2/4$. Therefore the $\gamma$-factor of the electron after one laser cycle is

$$\gamma_t = \sqrt{1 + \tilde{p}_{\parallel,t}^2 + \tilde{p}_{\perp,t}^2} \approx 1 + \tilde{p}_{\parallel,t}. \tag{104}$$

In this case, the average drift velocity in the longitudinal direction can be calculated as,

$$\frac{v_D}{c} = \frac{\tilde{p}_{\parallel,t}}{\gamma_t} = \frac{a_0^2}{4 + a_0^2}. \tag{105}$$

It's important to note that such a drift motion does not imply an energy transfer from the EM field to the electron. When the field is turned off, the electron returns to its initial velocity. It is possible to choose a proper co-moving average rest frame to vanish the drift velocity. The orbits form the famous figure-of-8 as shown in Figure 4.

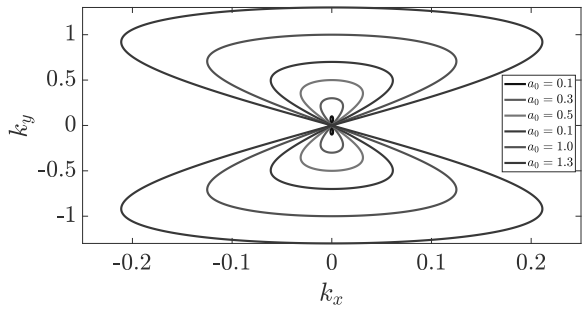


FIG. 4: Electron orbits with figure-of-8 in the average rest frame.

### 2.2 Free Electron in a Focused Laser Pulse

The analytical electron trajectories obtained in the previous section are valid under the assumption of plane waves. In reality, however, the laser pulses are usually approximated by a Gaussian beam profile both spatially and temporally as

$$E(y) = E_0 \frac{\exp[-ikx - \varphi(x)]}{w(x)} \exp[-\frac{r^2}{w(x)^2} - i\frac{\pi r^2}{\lambda R(x)}], \tag{106}$$

where $R(x)$ is the beam radius of curvature, $\varphi(x)$ is the Guoy phase shift, and $w(x)$ is the transverse spot size at a longitudinal position $x$. A Gaussian beam propagating in vacuum has the smallest spot size at the focal position, called the beam waist $w_0$. The spot size away from the focal position is given by

$$w(x) = w_0 \sqrt{1 + (\frac{x}{Z_R})^2}, \tag{107}$$

where $Z_R = \pi w_0^2/\lambda$ is the Rayleigh length. It indicates the distance after which the cross-beam area has doubled. The corresponding Gaussian beam profile according to the Rayleigh length is shown in Figure 5. It should be noted that the beam waist $w_0$ is different to the FWHM (Full Width Half Maximum) spot size, which is often used in describing the beam width. They have the following relation that $w_{FWHM} = \sqrt{2\ln(2)} w_0 \approx 1.177 w_0$.

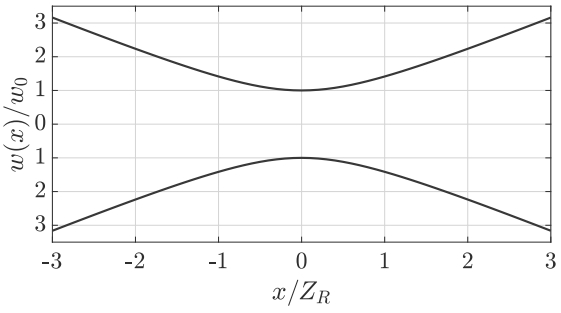


FIG. 5: Schematic of a Gaussian beam.

Unlike the plane wave, the laser intensity of the focused Gaussian beam is no longer spatially uniform. This makes the interaction of a single electron with the focused beam more complicated and more realistic. Taking the Taylor expansion of the electric field and cut off at the second order gives

$$E_y = E_0 \cos\phi + y \frac{\partial E_0}{\partial y} \cos\phi. \tag{108}$$

Similar to Eq. (91), the transverse velocity under the non-relativistic condition can be written as

$$\frac{\partial v_y}{\partial t} = -\frac{e}{m_e} E_y. \tag{109}$$

Taking the first order in Eq. (108), it is easy to get

$$\begin{cases} v_y^{(1)} = -\frac{eE_0}{m_e\omega}\sin\phi \\ y^{(1)} = \frac{eE_0}{m_e\omega^2}\cos\phi \end{cases} \tag{110}$$

Plugging $y^{(1)}$ into the second order condition gives

$$\frac{\partial v_y^{(2)}}{\partial t} = -\frac{e^2}{m_e^2\omega^2} E_0 \frac{\partial E_0}{\partial y}\cos^2\phi. \tag{111}$$

Averaging in the cycle of $\phi$ gives that,

$$f_p = m_e \frac{\partial v_y^{(2)}}{\partial t} = -\nabla\Phi_p, \tag{112}$$

where $f_p$ is the ponderomotive force applied on the electron based on the ponderomotive potential of

$$\Phi_p = \frac{e^2 E_0^2}{4m_e\omega^2}. \tag{113}$$

It is easy to see that the effect of the ponderomotive force is to transversely push the electrons away from the high intensity region to the low intensity region. Eqs. (112) and (113) also show that the ponderomotive force is independent of the positive or negative charge. Both electrons and ions are expelled away.

One may argue that the above derivation only valid in the non-relativistic condition. However, the relativistic ponderomotive force is also exists with a similar effect. To derive under the relativistic case, the total derivative of the momentum is rewritten as $d\mathbf{p}/dt = \partial\mathbf{p}/\partial t + \mathbf{v}\cdot\nabla\mathbf{p}$. Combining with Eqs. (81), (82) and (85), it gives

$$\frac{\partial \mathbf{p}}{\partial t} = -\mathbf{v}\cdot\nabla\mathbf{p} + \frac{e}{c}\frac{\partial \mathbf{A}}{\partial t} - \frac{e}{c}\mathbf{v}\times\nabla\times\mathbf{A}. \tag{114}$$

Using the vector identities, it is easy to get

$$\mathbf{v}\cdot\nabla\mathbf{p} = \frac{\nabla|\mathbf{p}^2|}{2\gamma m_e} - \mathbf{v}\times\nabla\times\mathbf{p}, \tag{115}$$

where $\gamma$ is the relativistic factor of the electron. Be careful to distinguish it from the $\gamma$ of the adiabatic index in Sec. I. Although, by historical convention in physics, they use the same symbols. Considering the fast oscillation of the electron motion, the corresponding momentum has the form as in Eq. (91). Therefore, it gives

$$\mathbf{v}\times\nabla\times\mathbf{p} = \frac{e}{c}\mathbf{v}\times\nabla\times\mathbf{A}, \tag{116}$$

which is actually eliminated with the $3^{rd}$ term on the RHS in Eq. (114). Thus the corresponding partial derivative of the momentum can be rewritten as

$$\frac{\partial \mathbf{p}}{\partial t} = -\frac{\nabla|\mathbf{p}^2|}{2\gamma m_e} + \frac{e}{c}\frac{\partial \mathbf{A}}{\partial t}. \tag{117}$$

Averaging in the laser cycle, it gives

$$f_p = <\frac{\partial \mathbf{p}}{\partial t}> = -m_e c^2 \nabla <\gamma>, \tag{118}$$

which is the expression of the relativistic ponderomotive force.

A typical case using numerical calculations to illustrate the effect of the ponderomotive force is shown in Figure 6. The black line is obtained under the condition of a plane wave laser pulse with a dimensionless amplitude of $a_0 = 3$ and a pulse length of $\tau_L = 30fs$. The trajectory basically follows the analytical solutions in Eq. (103) and has the similar shape as shown in Figure 3. The laser pulse is then replaced by a focused Gaussian beam with a beam waist of $10\mu m$, while keeping the pulse length and amplitude unchanged. As shown by the red line, the longitudinal motion of the electron in the focused beam is similar to the previous plane wave case. In the transverse direction, however, the electron drifts away, driven by the ponderomotive force, and never returns to its original axis. This transverse motion completely changes the electron dynamics.

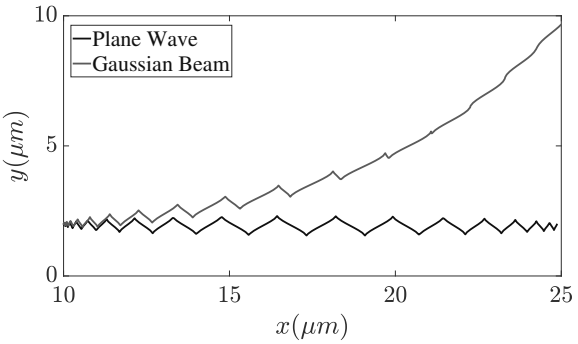


FIG. 6: Electron trajectory in a plane wave and Gaussian beam.

The ponderomotive force is important in the high-power laser-plasma interactions and the associated particle accelerations. By pushing the electrons into the low intensity region, it leads to many nonlinear effects including laser self-focusing, filamentation, cavity formation, and parametric instabilities. Although

the ponderomotive force applied on the ions might be negligible due to their heavy mass, the charge separation field resulting from the electron motion will affect the ions on a long time scale.

# III. Laser Wakefield Acceleration

The previous sections introduced the plasma collective oscillation and the ponderomotive force exerted on the particles by the EM field. On the basis of the above, in this section we begin our discussion of laser wakefield acceleration (LWFA).

A laser pulse pushes electrons away by the ponderomotive force when it propagates in an underdense plasma. The motion of ions is neglected in this section due to their large mass. In other words, ions are considered as a background with uniform and steady density distributions, which is common in LWFA research. The positive charge distribution provides a restoring force to attract the electrons back and so the electrons will oscillate around the ions. The laser propagates in the underdense plasma with the group velocity of $v_g \approx \sqrt{1-\omega_{pe}^2/\omega_L^2}$ and continuously expel the electrons on its path. Thus a plasma wave is driven by the laser pulse with the a phase velocity equal to the laser group velocity. It's easy to know that the wavelength of the plasma wave is $\lambda_p = 2\pi v_g/\omega_{pe}$. The plasma wave generates a longitudinal electric field behind the laser pulse and allows the electrons to be accelerated along the laser direction. The laser induced plasma wakefield and the corresponding electron acceleration principles are shown in Figure 7 from Ref. [3].

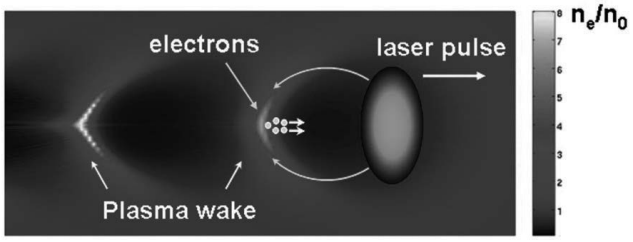


FIG. 7: The schematic of LWFA. Figure from Ref. [3].

The idea was first proposed by Tajima and Dawson in 1979 [4] and after that it soon became a subject of great interest. Remarkable progress has been achieved in the past decades accompanied with the development of high-power laser technology. The plasma wave supports large electric fields reaching 100 GV/m, which makes the potential compact accelerator to be possible. Various mechanisms for electron injection, laser pulse guiding and beam quality improvement have been proposed and demonstrated in the past decades. Based on all of these efforts, electron beams up to 8 GeV with the charge quantity of tens pico-Coulomb have been addressed in experiments [5, 6]. Although the accelerated electron beam quality is still not as optimized as the conventional accelerators, quasi-monoenergetic beams with energy spread less than several percent can be achieved now.

### 3.1 Linear and Nonlinear plasma waves

Before discussing the details of LWFA, it is important to understand how such large amplitude waves are generated in the plasma. As mentioned in Eq. (79), a low intensity EM field propagates in the underdense plasma without significant disturbing. It is due to the fact that the electron momentum gained from the laser pulse is small enough ($p_e << m_e c$) and the linearization in Eqs. (76) are satisfied. However, according to the discussion of single electron dynamics in the EM field in Sec. II, the electron momentum in the laser field becomes non-negligible when the laser intensity is sufficiently high. Thus the electron oscillations and the corresponding electron plasma waves become important.

Assume a laser pulse propagates in the underdense plasma along $x-$direction and polarized along the $y-$axis, which can be expressed as,

$$\mathbf{a} = \hat{a}(x,t)\cos(k_0 x - \omega_0 t)\hat{e}_y, \tag{119}$$

where $k_0$ and $\omega_0$ are the laser wave vector and frequency, and $\hat{a}$ is the envelope function representing the longitudinal shape of the pulse. Considering a Gaussian pulse so that the shape function can be expressed as

$$\hat{a}^2(\zeta) = a_0^2 \exp(-\zeta^2/L_0^2), \tag{120}$$

where $\zeta = x - v_g t \approx x - ct$ with $v_g$ being the laser group velocity, $L_0$ is the pulse length, and $a_0$ is the peak amplitude. The dimensionless amplitude has the following relation with the laser intensity $I_L$ and the laser central wavelength $\lambda_L$,

$$a_0 = 8.6 \times 10^{-10}\sqrt{I_L[\mathrm{W/cm^2}]\lambda_L^2[\mu\mathrm{m}]}. \tag{121}$$

The advantage of using $\zeta$ is that it allows the Eulerian transformation and gives $\partial/\partial x = \partial/\partial\zeta$ and $\partial/\partial t = -c\partial/\partial\zeta$, so that the second-order derivative becomes $\partial^2/\partial x^2 = \partial^2/\partial\zeta^2$ and $\partial^2/\partial t^2 = c^2\partial^2/\partial\zeta^2$.

The particle motion is dominated by the electric field and the laser ponderomotive force in Eq. (118):

$$\frac{\partial \mathbf{p}}{\partial t} = -e\mathbf{E} - m_e c^2 \nabla\gamma. \tag{122}$$

Combined with Poisson's equation and the continuity equation, the full electron plasma waves can be described. Rewrite the equations in the new coordinate system gives,

$$\begin{cases} -\frac{\partial p}{\partial \zeta} = \frac{e}{c}\frac{\partial \Phi}{\partial \zeta} - m_e c \frac{\partial \gamma}{\partial \zeta} \\ \frac{\partial^2 \Phi}{\partial \zeta^2} = -\frac{\partial E}{\partial \zeta} = 4\pi e n \\ -\frac{\partial n}{\partial \zeta} + \frac{(n\beta_p)}{\partial \zeta} = 0, \end{cases} \tag{123}$$

where $\beta_p = v/c$ is the normalized velocity. $\beta$ can be eliminated with the relation of $\gamma^2(1-\beta_p^2) = (1+\phi)^2$, in which the normalized potential $\phi = e\Phi/m_e c^2$ is used. Thus the Poisson's equation can be rewritten as

$$\frac{\partial^2 \phi}{\partial \zeta^2} = -\frac{k_p^2}{2}[\frac{1+a^2}{(1+\phi^2)} - 1], \tag{124}$$

where $k_p = \omega_{pe}/c$.

Considering the electrons motion along the longitudinal direction, and neglect the role of radial electric field. In this case, the wakefield potential is only the function of $x$ and $t$, i.e. $\phi = \phi(x,t)$. For simplicity, we assume the laser pulse does not change during its propagation. Therefore, the corresponding wakefield is also stationary and it allow us to use the law of energy conservation. Plasma ions are assumed to be immobile, since the typical time for ion motion is much longer than the pulse duration, i.e. $\tau << \omega_{pi}^{-1}$, where $\omega_{pi}^{-1} = (4\pi n_i e^2/m_i)^{1/2}$ is the ion plasma frequency. The electron fluid is cold, as $v_{osc} = eE_L/(m_e\omega_0) >> v_{th} = (k_B T_e/m_e)^{1/2}$. In the limit of $\phi < 1$ and $a_0 < 1$, Eq. (124) can be further simplified to

$$(\frac{\partial^2}{\partial \zeta^2} + k_p^2)\phi = \frac{k_p^2 a^2}{2}. \tag{125}$$

The analytical solution for Eq. (125) can be given as,

$$E_x = \frac{2\pi^2 \phi k_p}{4\pi^2 - k_p^2 \zeta_L^2}[\sin k_p(\zeta - \zeta_L) - \sin k_p \zeta]. \tag{126}$$

The corresponding solution is shown in Figure 8. It clearly shows that the sine waves of the electron density oscillation and the longitudinal electric field are formed behind the laser pulse. However, in the case of a relative strong laser pulse, the equation describe the plasma wave becomes,

$$\frac{\partial^2 \phi}{\partial \zeta^2} = k_p^2 \gamma_p^2 [\beta_p (1 - \frac{1+a^2}{\gamma_p^2 (1+\phi)^2})^{-1/2} - 1]. \tag{127}$$

Noted that Eq. (127) is actually the NONLINEAR plasma wave equation, which is valid for the case of

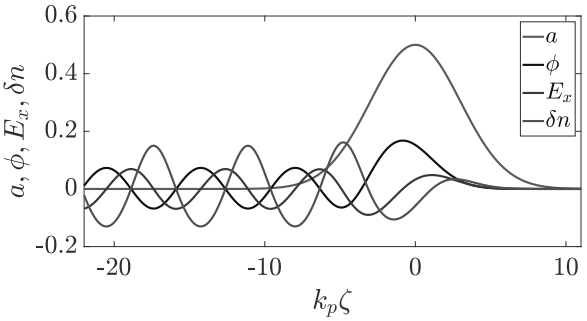


FIG. 8: Solutions for the case of $a_0 = 0.5$.

$a_0 > 1$ and $\phi > 1$, i.e. for relativistic laser intensities with $I_L > 10^{18}\mathrm{W/cm}^2$. A more rigorous derivation should take the plasma temperature into account. This is because the plasma pressure has a confining effect on the density distribution and the thermal electrons are more easily trapped by the wake field. However, the analysis is complicated and details can be found in Ref. ([7]).

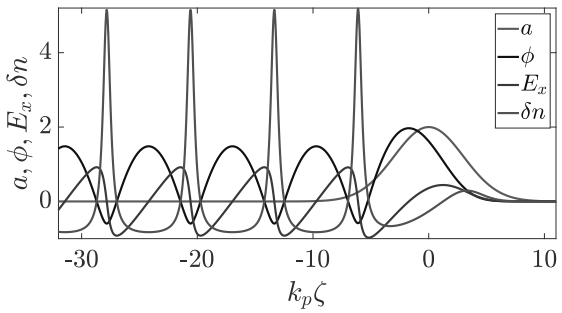


FIG. 9: Solutions for the case of $a_0 = 2$.

The numerical solution for the case of $a_0 = 2$ is presented in Figure 9. The plasma parameters here are exactly the same as in the previous case of $a = 0.5$. The shape of the density perturbation and the longitudinal electric field are no longer sinusoidal. The strength of the electric field is also much stronger than in the previous case.

By using the numerical tool of particle-in-cell (PIC) simulation, the electron density distribution driven by a short pulse laser is shown in Figure 10, where the laser amplitude is about $a_0 = 1.8$. A 2D wakefield structure is presented. The black line represents the transverse electric field, the white line is the density profile and the red line is the longitudinal electric field. All the lines are cut along the laser axis. The simulation results are similar to the solutions presented in Figure 9. In each period of the electric field, half of the wavelength is able to accelerate electrons in the forward direction.

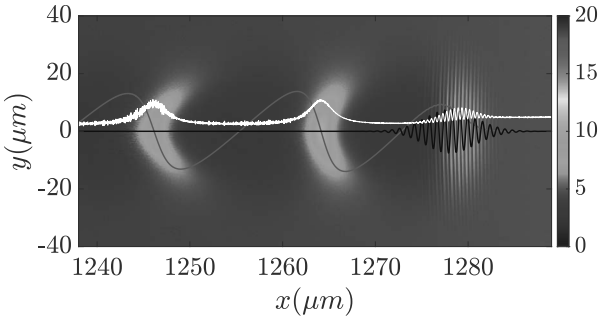


FIG. 10: 2D wakefield structure via PIC simulation.

### 3.2 Wave Breaking

As mentioned above, the same plasma produces the wakefield with different amplitudes when the pump laser is changed. This raises the question of what is the maximum limit of the wakefield. The wakefield strength as $a_0$ increases is shown in Figure 11 based on the numerical solution of Eq. (127). The structure of $E_x$ transits from a sine wave to a sawtooth wave. It indicates that the fluid velocity at the tail of the wave becomes faster as the amplitude increases.

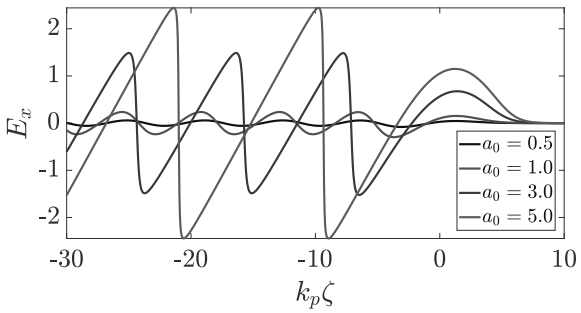


FIG. 11: Wakefield strength according to $a_0$.

To maintain a coherent wave structure, fluid dynamics dictates that the velocity of the fluid cannot exceed the phase velocity of the wave. In the case of the wakefield, if the electrons at the tail of the wake wave are moving faster, then the electron charge sheets will cross and the wave will lose its coherence, often referred to as 'wave breaking'. First consider the linear plasma wave case with $\delta n = n_0 \sin(k_p\zeta)$ and $E_x = 4\pi e \int \delta n d\zeta$. It is easy to obtain the so called 'cold wavebreaking limit' as

$$E_0 = \frac{m_e c\omega_{pe}}{e} \approx 0.96\sqrt{n_e[cm^{-3}]}(\mathrm{V/cm}). \qquad (128)$$

By plugging $n_e \sim 10^{18} cm^{-3}$ into Eq. (128), the maximum amplitude is about GV/cm, which is three orders of magnitude higher than that of the conventional accelerator.

In the case of nonlinear plasma wave, the maximum amplitude is further increased by the $\gamma_p$ factor as

$$E_{WB} = \sqrt{2(\gamma_p - 1)}\frac{m_e c\omega_{pe}}{e}. \qquad (129)$$

For a laser pulse with $\gamma_p = 50$, the maximum wakefield amplitude becomes 10 time higher than the cold wavebreaking limit. By checking the density perturbations in Figure 12, one find that the density approaches $n \sim \infty$ and the peak becomes singular with the increase of $a_0$, which indicates a breakdown of the fluid equation. Similar to the discussion of thermal effect in Eq. (127), the pressure will also reduce the maximum amplitude of the wakefield. The details can be found in Ref. ([8])

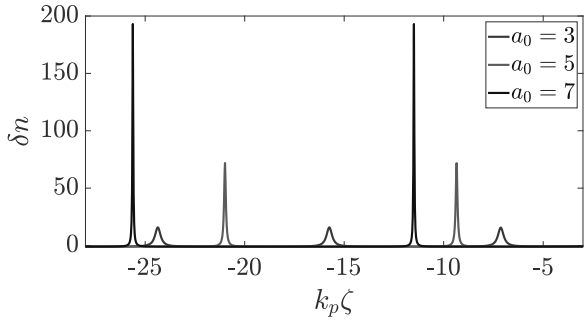


FIG. 12: Density perturbation according to $a_0$.

So far, the considerations are focused on the wave breaking in the longitudinal direction. The particles at the tail of the wakefield, which experience the wave breaking, enter the strong acceleration phase of the wakefield. This is the so called electron self-injection regime in LWFA which requires a strong laser field. In fact, the transverse structure and the curvature of the wakefield also cause the transverse wave breaking. The corresponding analysis and detail discussions can be found in Ref. ([9]).

### 3.3 Injection Scheme

To realize high energy electron acceleration, the strong wakefield alone is not sufficient. The seed electrons should be properly injected and trapped by the wakefield. One of the most important steps is the electron injection. Consider an electron moving in the wakefield with the phase velocity of $v_p$. The electron position can be expressed by $\zeta$ and its corresponding phase in the field is $\varphi = k_p\zeta$. According to the previous discussion, $-\pi < \varphi < 0$ is the acceleration phase while $0 < \varphi < \pi$ is the deceleration phase. If the electron's initial velocity is not relativistic, it will continuously shift back relative to the wakefield. If the electron velocity at the phase of $\varphi = -\pi$ is still

smaller than $v_p$, it will leave the acceleration phase and enter the next deceleration phase. In another word, only the electron with its velocity higher than $v_p$ at $\varphi = -\pi$ can be trapped and accelerated by the wakefield.

To discuss the trapping and injection condition, consider the Hamiltonian of an electron as

$$H = \sqrt{1+\tilde{p}^2} - \beta_p \tilde{p} - \phi(\zeta), \tag{130}$$

where $\tilde{p}$ is the normalized momentum. After the Canonical transformation, the Hamiltonian becomes

$$H(\gamma, \varphi) = \gamma(1 - \beta\beta_p) - \phi(\varphi). \tag{131}$$

The electron motion inside the phase space $(\tilde{p}, \zeta)$ can be solved by the Hamilton's equations,

$$\begin{cases} \frac{d\zeta}{dt} = \frac{\partial H}{\partial \tilde{p}} \\ \frac{d\tilde{p}}{dt} = -\frac{\partial H}{\partial \zeta} \end{cases} \tag{132}$$

A typical solution with the initial condition of $\phi_0 = 0.1$ and $\gamma_p = 10$ was given in Ref. [10] as shown in Figure 13.

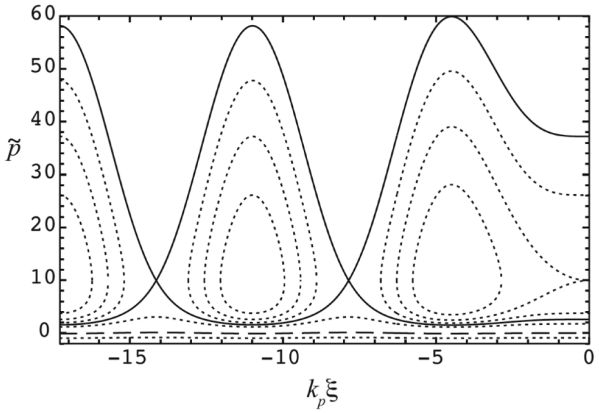


FIG. 13: Single particle orbits in phase space. Figure from Ref. [10].

The solid lines are the so-called separatrix, which separates the trapped and untrapped electrons. The electrons slide back with respect to the plasma wave at an initial velocity $v_x 0$. If $v_x 0$ is too low, the electron cannot gain sufficient momentum at the phase transition position, i.e. $\varphi = -\pi$. Only the electrons whose orbits are inside the separatrix could have enough velocity to catch the plasma wave and be continuously accelerated in the forward direction. It indicates that the cold electrons in the background plasma cannot be injected into the wakefields. In order to get high efficiency acceleration, many injection mechanisms have been proposed in the past decades. In general, there are two ways to improve the injection, either by increasing the electron velocity or by decreasing the phase velocity of the plasma waves. The main injection mechanisms including self-injection, external injection, optical injection, ionization injection, and density downramp (shock) injection.

### *3.3.1 Self-injection*

Self-injection means that the background electrons of the plasma are captured and accelerated by the plasma waves without any external beam source or other operations. As mentioned above, the electron self-injection occurs with the longitudinal wave breaking. The advantage of self-injection is that it is easy to be realized. Self-injection is always used in the early stages of LWFA experiments. A typical self-injection case is presented in Figure 14 via the PIC simulations. Here the electron plasma density is $n_0 = 10^{19}\text{cm}^{-3}$ and the dimensionless amplitude of the laser pulse is $a_0 = 10$. According to Eq. (129), the corresponding wave breaking field is about $E_{WB} \approx 15$ GV/cm, which is consistent with the longitudinal electric field (red line) shown in Fig. 14(a). As a result, the plasma wave breaks rapidly, as shown in Fig. 14(b). An electron bunch with with a transverse size of $4\mu m$ is injected at the tail of the bubble structure, in which the transverse injection occurs together with the longitudinal injection. Noted that the amplitude of the plasma wave decreases once the wave breaks. Further electron injection is then stopped. In Fig. 14(c), a large injected bunch can be clearly seen inside the bubble. Based on the color of the beam density, it is easy to know that the charge of the bunch is large. The wakefield has already been disturbed by the Coulomb field from the bunch. The over charge loading is negative in producing the beam with small energy spread.

Although the setup for self-injection is simple, as a critical phenomenon at the high intensity, the injection is difficult to be controlled precisely and the corresponding beam quality is unstable. Normally due to the consecutive injection, the energy spectrum of the accelerated electron beam is quite broad. In addition, self-injection has a relatively low efficiency and the process is stochastic. If more control over the injection process is demanded in order to improve the beam quality, self-injection with wave breaking is not the optimised solution.

### *3.3.2 External Injection*

In principle, all electrons experience the same longitudinal electric field with the same phase only if

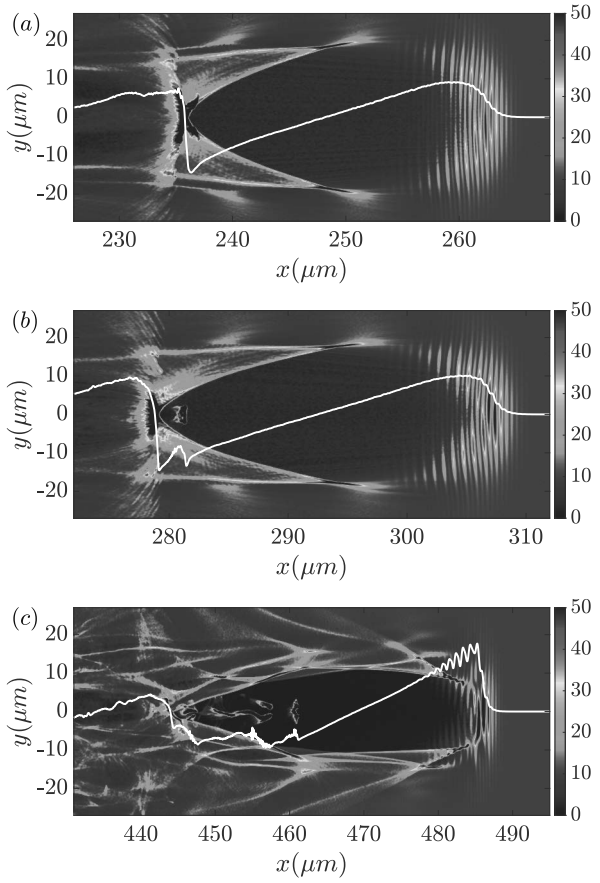


FIG. 14: The typical self-injection process obtained via PIC simulation.

the electron injection process is localized in time and space. In this case, the initial mono-energetic beam is preserved. One of the choice is the external injection method, in which the electron beam may originate from the conventional accelerator. Normally the electrons source from the RF accelerator has stable beam pointing and the narrow energy spread as an ideal external source. However, such the two stage acceleration is difficult in alignment because of the micrometre size of both the beams and the wake structures. The successful cases have been demonstrated at BELLA of LBNL [11] and CERN [12].

A typical setup is shown in Figure 15 from Ref. [13]. A cathode of the RF photogun is in front of the entrance of the plasma channel to allow the laser pulse propagation. A pulsed solenoid with the magnetic field of 0.68 T is used to focus the electrons into the plasma channel. The RF photogun produces electrons with the energy of several MeV as the external source. In their experiments, the pico-Coulomb electron beam was accelerated from 3 MeV to more than 900 MeV with $\sim$ 5% energy spread in bunches of 8 fs.

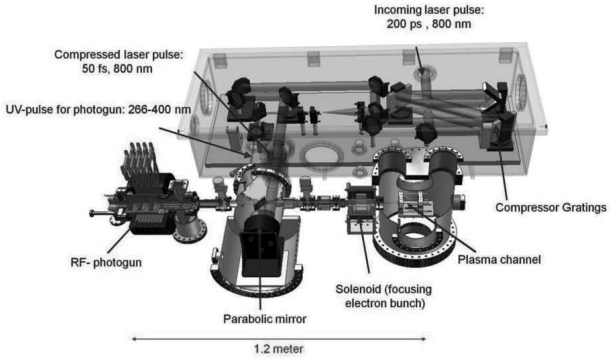


FIG. 15: The typical setup of external injection using an RF photogun for external electron source. Figure from Ref. [13].

### *3.3.3 Optical Injection*

Optical injection was first proposed in 1996 with two orthogonal laser pulses [14]. The first laser pulse is used to excite the wakefield in the plasma. The second laser pulse in the perpendicular direction provides a local perturbation to change the trajectory of some of the electrons so that they can be accelerated and trapped by the plasma wave. In this case, the transverse ponderomotive force from the second laser pulse kicks the electrons. In fact, such local perturbation of the electron trajectories for the injection assistant can be achieved by ponderomotive force, standing wave and electron heating. The corresponding mechanism is explained in Figure 16 from Ref. [3].

Esarey et al. proposed to use a beat wave for electron injection via the laser pulses in a counter-propagating geometry [15]. The interference of the main pulse and the second pulse creates a beatwave pattern, which heats the local electrons from the plasma background. The force associated with such the beatwave is much stronger than the ponderomotive force from the pumping laser. Thus the intensity of the second pulse can be significantly reduced.

Optical injection has been demonstrated in both simulations and experiments. One of the advantages is that the optical injection with colliding pulse allows to control the injection phase precisely which is realized by changing the time delay between the two pulses. This makes the electron beam energy controllable and the energy spread relatively small. Therefore, optical injection has a high demanding in the spatial and temporal synchronization in experiments, which is the main challenge for this method.

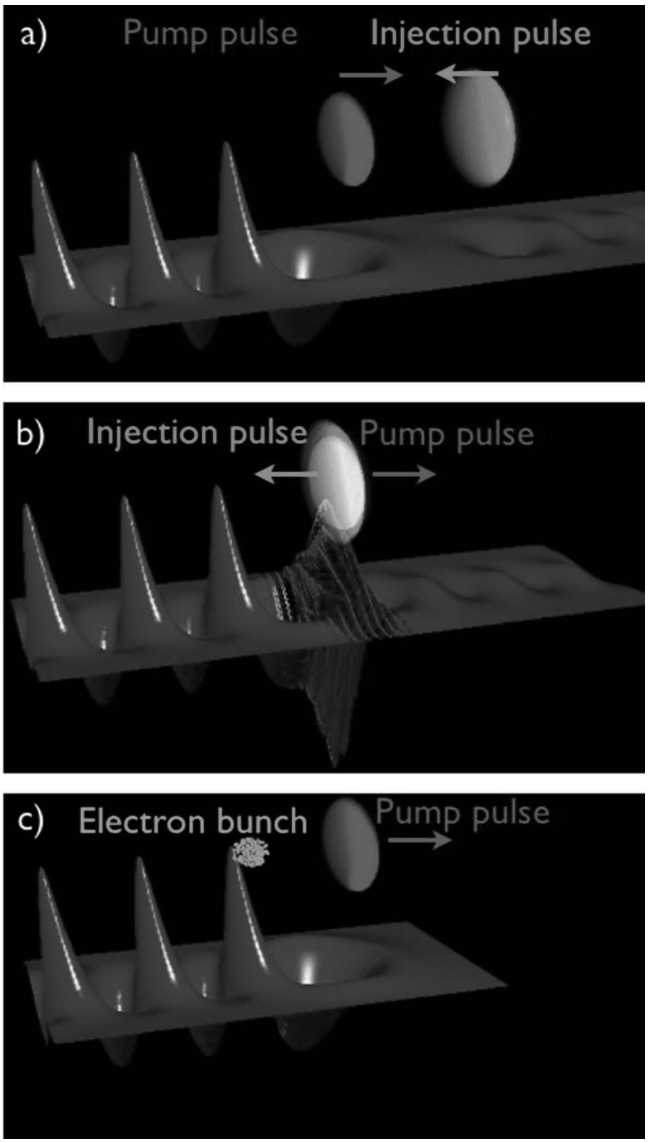


FIG. 16: The principle of optical injection. Figure from Ref. [3].

### *3.3.4 Ionization Injection*

Ionization injection utilizes the different ionization potential energies of the electrons on different shells. As the laser pulse propagates through the plasma, the electrons on the outer shell with low ionization energy are ionised first to form the background plasma. The plasma waves are thus formed by these background electrons. Since the laser intensity is not strong enough to drive the wave breaking and self-injection, the background electrons only oscillate with the plasma waves without injection. Now the ions in the plasma still contain the electrons on the inner shells. If the electrons are released during the acceleration phase of the plasma waves, they can be captured and accelerated further. The idea was first proposed by Chen et al. in 2006 [16].

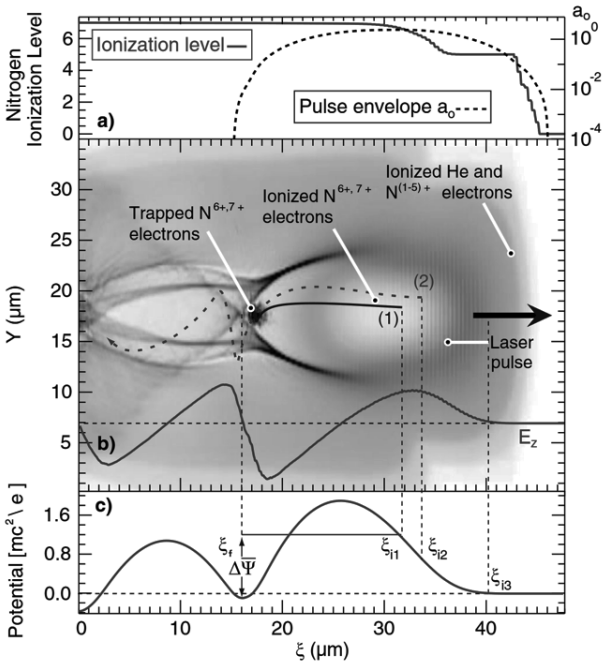


FIG. 17: The principle of ionization injection. Figure from Ref. [17].

It is easy to understand that ionization injection usually requires the gas of high-Z atoms, such as Nitrogen, or a mixture gas with both high-Z and low-Z elements. One of the key factor is to proper calculate the ionization process. Normally the field ionization and tunnel ionization models are considered. A typical case was shown in Figure 17 from Ref. [17]. The ionization level of N with respect to the laser dimensionless amplitude is shown in Fig. 17(a). The electrons from $N^{1+}$ to $N^{5+}$ can be easily ionized and form the background plasmas. For the electrons from $N^{6+}$ to $N^{7+}$, only the intensity at the pulse center can ionize where the electric field of the laser is close to the ionization field. Not all the electrons can be injected into the plasma wave, even if their initial positions are similar, as shown in Fig. 17(b). The electron represented by the dashed red line slips backwards with respect to the wakefield. However, the electron represented by the solid black line, whose initial position is just $2\mu m$ away from the previous one, can be trapped and accelerated in the wakefield. The different results depend on the electric potential at the ionization location $\psi_0$. Theoretical research shows that the trapping condition in ionization injection is determined by the potential difference of

$$\Delta\Psi = \psi_0 - \psi_{min} > \frac{m_e c^2}{e}, \tag{133}$$

where $\psi_{min}$ is the minimum of the electric potential.

Ionization injection has the advantages of low laser intensity threshold and high injection efficiency. For a typical $800nm$ laser, the amplitude threshold for injection is about $a_0 \leq 1.7$. It has become one of the main methods in LWFA. However, ionization injection is a consecutive injection process. The beam energy spread is usually quite broad. To improve the beam quality, it is necessary to cutoff the injection which is called Self-truncated ionization injection as proposed in Ref. [18]. The corresponding energy spread can be controlled to less than 10%.

### *3.3.5 Density Downramp Injection*

In the above injection mechanisms, the main ideas are focused on increasing the electron velocity to catch up the plasma wave. As mentioned above, electron injection can also be achieved by decreasing the phase velocity of the plasma waves, which has been realized in density downramp injection. The wavelength of the plasma wave is inversely proportional to the local plasma density as

$$\lambda_p = \frac{2\pi c}{\omega_{pe}} \approx \sqrt{\frac{\pi m_e c^2}{ne^2}}. \tag{134}$$

Considering that the plasma density gradually decreases in the longitudinal direction, the plasma wavelength will increase, i.e. the corresponding phase velocity of the plasma wave will decrease. Thus, the electrons located at the tail of the plasma wave will satisfy the injection condition. Density downramp injection was first proposed in 2001 [19].

In experiments, the density transition region is normally formed when a supersonic gas stream collides with a razor blade as seen in Fig. 18(a). A typical density profile with such the setup is shown in Fig. 18(b). The red part is the density downramp region which is very sharp. Such the transition region is actually a shock in density distributions. Therefore, the downramp injection is often called as 'shock injection'.

By 2D PIC simulation, the variation of the plasma wave and the electron injection can be reproduced. Here we focus on the situations before and after the shock as shown in Fig. 19(a) and (b), respectively. The size of the first plasma wave is about $18\mu m$ before the shock. It extends to more than $22\mu m$ after the shock and some of the electrons at the tail of the first bubble have been injected into the acceleration phase as seen in Fig. 19(b). Since the density transition (shock) is very sharp, the injection process which only occurs at the shock can be controlled in a short time. Therefore the injected beam length is also very short, which results that most of the electrons locate at the same acceleration phase. Fig. 19(c) shows the

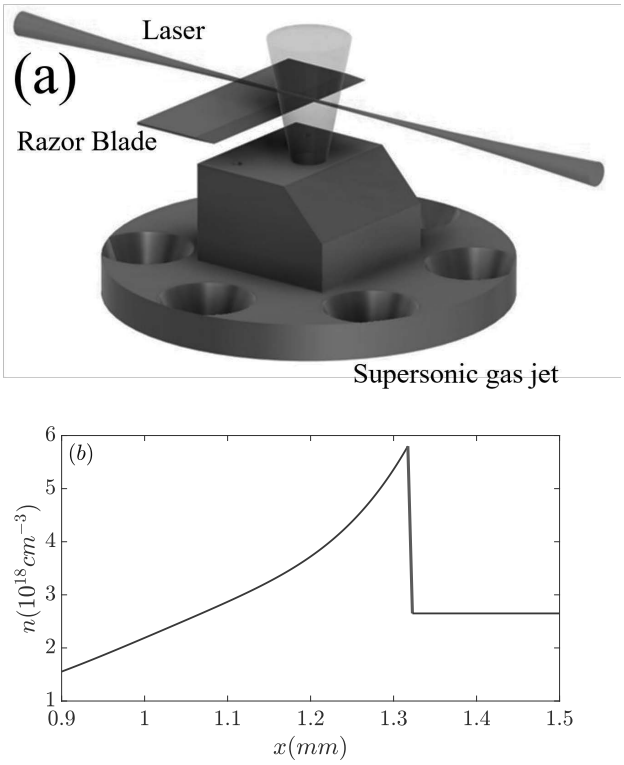


FIG. 18: (a) Schematic of the shock injection experiment setup. (b) The longitudinal density profile in a typical case of density downramp injection.

electron beam accelerated till about $3mm$ and the beam length is about $1.5\mu m$. The energy spectrum in this case is narrow and the energy spread becomes $\Delta E/E \sim 1\%$.

The advantages of density downramp injection is its high beam quality. However, the stability and reproducibility are still extremely challenging. Due to the highly non-linear injection and acceleration processes, there are numerous parameters that influence the electron dynamics. One of the main instabilities come from the supersonic gas nozzle. When the high velocity flow shear is combined with a nozzle wall, the corresponding velocities are significantly reduced due to the boundary effect. Such a boundary effect is not only a singularity in the flow field that provides the seed for the vortex and turbulence, but also partially blocks the nozzle cross-section, resulting in significant variations in gas pressure. As a result, the gas target becomes unstable and the laser focal position may exceed the allowable misalignment. Recent research from SANKEN at Osaka University [20, 21] indicates that the stilling chamber with a modified converging–diverging nozzle can effectively dissipate the nonlinear instabilities originated from the fluid boundary effects.

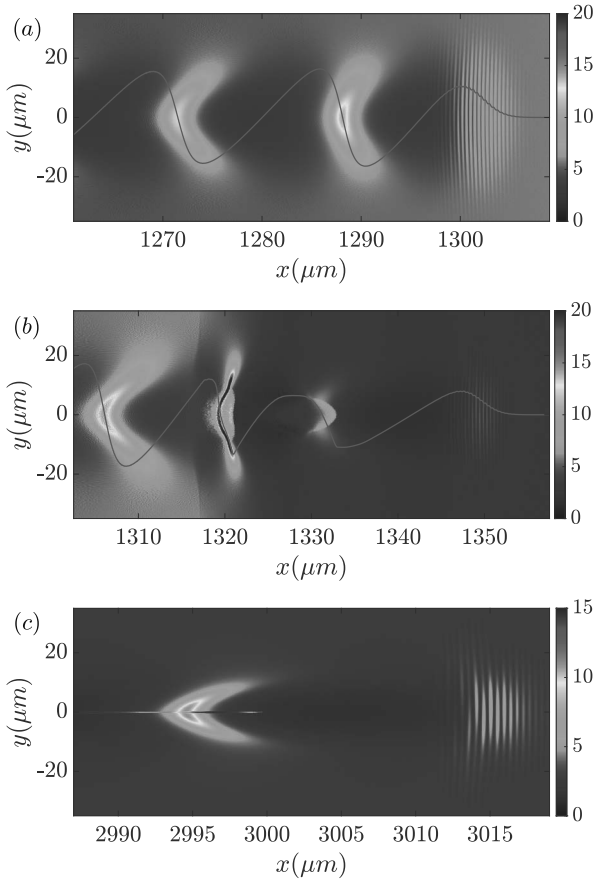


FIG. 19: The electron density distributions before and after the shock, where the shock locates at $x = 1.31mm$.

### 3.4 Scaling Law and Acceleration Limit

The energy gain in LWFA is affected by several factors including the pumping laser energy, the laser diffraction effect, the electron beam phase shift and the beam charge. Understanding these principles is important for better design of the LWFA setup. In this section, the acceleration limit and the corresponding energy scaling law will be discussed which may provide a rough estimation of the acceleration effect.

#### *3.4.1 Rayleigh Diffraction and Self-focusing*

In the laser-plasma interactions, it would be ideal if the laser pulse could propagate over long distances at high intensity. For a Gaussian laser pulse in vacuum, the high intensity can be maintained within a Rayleigh length due to the diffraction effect. The corresponding intensity is given by

$$I(r,x) = I_0(\frac{w_0}{w(x)})^2 \exp[\frac{-2r^2}{w(x)^2}], \qquad (135)$$

where the definition of the Gaussian beam is the same with Eq. (106). However, in the case of a laser propagating in an underdense plasma, it is possible to confine the laser intensity by the plasma focusing effect. This allows the laser to keep at a high intensity over a distance that is much longer than the Rayleigh length in a vacuum. Such the self-focusing effect can be well explained via a geometric optics scenario in Figure 20 from Ref. [2].

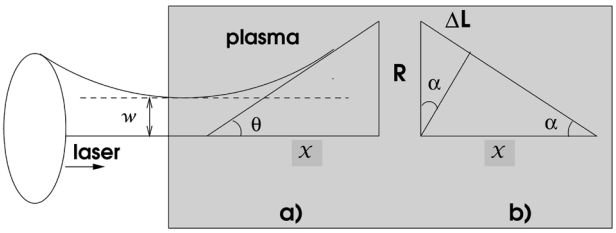


FIG. 20: Geometry of a diffraction and focusing Gaussian beam. Figure from Ref. [2].

The dimensionless amplitude of the laser has a Gaussian profile in the transverse direction as $a(r) = a_0 \exp(-r^2/2w_0^2)$. The focal position is inside the plasma as shown in Fig. 20(a). Without the consideration of the nonlinear focusing effect, the laser pulse will diffract with a divergence angle of

$$\theta = \frac{dR}{dx} = \frac{w_0}{Z_R} = \frac{2}{k_L w_0}, \qquad (136)$$

where $k_L = 2\pi/\lambda_L$ is the wave number of the laser pulse. According to the dispersion relation in Eq. (79), the refractive index of plasma can be defined as:

$$\eta = \frac{ck_L}{\omega_L} = \sqrt{1 - \frac{\omega_{pe}^2}{\omega_L^2}}, \qquad (137)$$

where the electron plasma frequency is assumed to be uniform. As mentioned above, the laser ponderomotive force transversely push the electrons with different strength. In the case of high intensity, the electrons gain different momentum along the transverse direction, resulting in a different relativistic factor. When relativistic effects are taken into account, the electron plasma frequency is no longer uniform in the transverse direction due to the different mass of the electrons. Thus Eq. (137) should be rewritten as

$$\eta(r) = \sqrt{1 - \frac{\omega_{pe}^2}{\omega_L^2 \sqrt{1 + a(r)^2/2}}}. \qquad (138)$$

Now the refractive index $\eta(r)$ has reached its maximum value along the axis ($r = 0$), indicating that the

plasma is analogous to a focusing lens as $d\eta/dr < 0$. The phase velocity of the wave fronts propagating in such the medium can be described as

$$v_p(r) = \frac{c}{\eta(r)} \approx c[1 + \frac{\omega_{pe}^2}{2\omega_L^2}(1 - \frac{a(r)^2}{4})]. \quad (139)$$

The phase fronts on the optical axis travels slower than that on the lateral as shown in Figure 21 from Ref. [2].

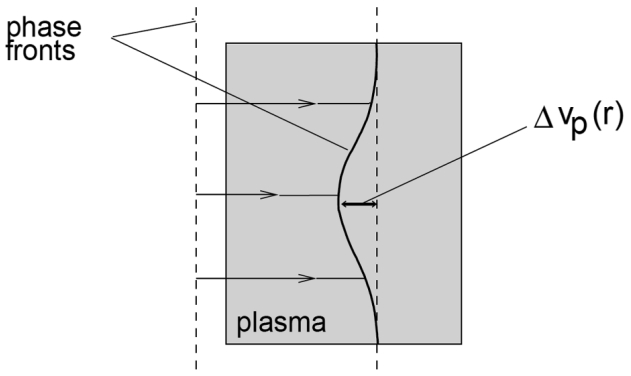


FIG. 21: Phase front shift in the transverse direction. Figure from Ref. [2].

The velocity difference is given by

$$\Delta v_p(r) = \frac{\omega_{pe}^2}{8\omega_L^2} a_0^2 \exp\frac{-r^2}{w_0^2} c. \quad (140)$$

The corresponding converging angle is $\alpha = \Delta v_p(r)t/R$ referring to Fig. 20(b). It is easy to obtain that $\alpha_{max} = \sqrt{\Delta v_p(0)/c}$. By balancing the converging angle with the divergence angle in Eq. (136), the self-focusing threshold can be expressed as

$$a_0^2 \leq 8(\frac{c}{\omega_{pe}} w_0)^2. \quad (141)$$

The laser power is proportional to $a_0^2$ as $P_L = \pi a_0^2 w_0^2$. Then the corresponding threshold of laser power for self-focusing is $P = 8(\omega_L/\omega_{pe})^2$(GW). It should be noted that this is not accurate, as the beam profile and electron dynamics have not been taken into account. According to a more rigorous derivation via the nonlinear Schrödinger equation, the accurate critical power for self-focusing is expressed as

$$P_{cr} = 17.5(\frac{\omega_L}{\omega_{pe}})^2(\text{GW}). \quad (142)$$

For further details regarding the derivation, please refer to Ref. [2].

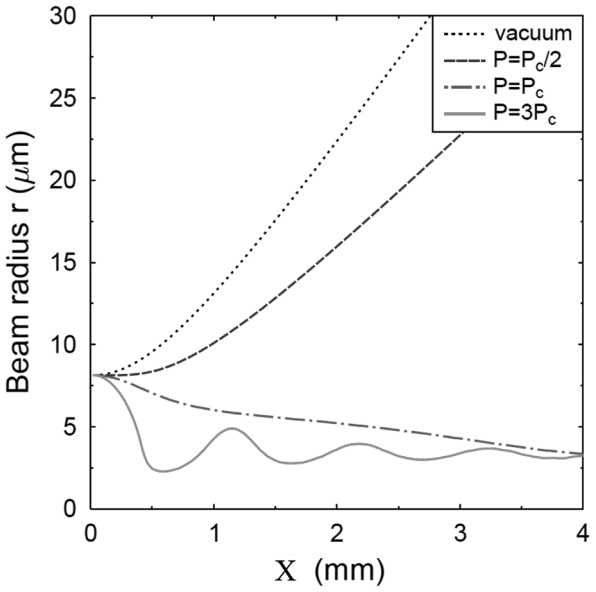


FIG. 22: The beam radius with respect to different power. Figure from Ref. [2].

Numerical simulations have proved the self-focusing effect with respect to the laser power. As seen in Figure 22, once the laser power exceeds the critical power of $P_{cr}$, the transverse beam size no longer increases even the propagation length is already much longer than the Rayleigh length.

Self-focusing is a crucial phenomenon in LWFA, as it significantly extends the laser-plasma interaction length. For a typical gas plasma with the density of $10^{18}$cm$^{-3}$, the corresponding critical power is about 18 TW. Most of the modern high power laser facilities are capable of exceeding the threshold. The acceleration length with self-focusing typically reaches several millimetres, whereas the Rayleigh length for a focused laser beam is approximately one millimetre. In order to achieve a longer acceleration length on a centimetre scale, it is necessary to employ a waveguide such as a discharged capillary. This also serves to mitigate diffraction, thereby increasing the acceleration length. Further details regarding the capillary plasma channel can be found in the successful experiments referenced in Refs. [22–24].

### *3.4.2 Pump Depletion Length*

The energy of plasma waves is derived from the driving laser pulse. It is evident that the acceleration process ceases when the pumping laser no longer possesses sufficient intensity to excite wakefields. Therefore, the so-called 'pump depletion length' can be estimated as the distance over which the laser pulse will transfer all its energy to the plasma wakes. As-

suming the depletion length is $L_{pd}$ and the average field energy density of wake is $E_{WB}^2/8\pi$, where $E_{WB}$ should be discussed under non-relativistic and relativistic condition according to Eq. (128) and Eq. (129), respectively. Thus the depletion condition can be expressed as

$$U_L \approx \frac{E_{WB}^2}{8\pi} L_{pd} w_0^2, \tag{143}$$

where $U_L$ is the laser pulse energy. The analytical solution in the 1D limit was given in Ref. [25, 26] as

$$L_{pd} = \frac{\lambda_p^3}{\lambda_L^2} \times \begin{cases} \frac{2}{a_0^2} & if \;\; a_0^2 << 1 \\ \frac{\sqrt{2}a_0}{\pi} & if \;\; a_0^2 >> 1 \end{cases} \tag{144}$$

It can be observed that the pump depletion length in the non-relativistic case is of a considerable length. In the relativistic case, the decrease of the length is rapid due to the significant enhancement of wakefield strength.

### *3.4.3 Dephasing Length*

As previously stated in Sec. (3.3), the wakefield has both the acceleration phase ($-\pi < \varphi < 0$) and deceleration phase ($0 < \varphi < \pi$). A highly relativistic electron will reach the phase transition point after propagating a certain distance with a velocity exceeding the phase velocity of the wakefield. The time it takes the electron to move half a plasma wave out of phase is

$$t_d = \frac{\lambda_p}{2} \frac{1}{(v_e - v_p)}, \tag{145}$$

where $v_e$ and $v_p$ are the electron velocity and the wake phase velocity, respectively. Similar to the pump depletion length, it should be discussed under non-relativistic and relativistic conditions separately as

$$L_d = \frac{\lambda_p^3}{2\lambda_L^2} \times \begin{cases} 1 & if \;\; a_0^2 << 1 \\ \frac{\sqrt{2}a_0}{\pi N_p} & if \;\; a_0^2 >> 1 \end{cases} \tag{146}$$

where $N_p$ represents the number of plasma periods behind the drive laser pulse.

### *3.4.4 Scaling Laws*

The scaling law for the energy gain in LWFA is determined by the bottle neck of the aforementioned lengths. Under the non-relativistic case, the pump depletion length is the longest one of the limiting factors so that the following relation is satisfied

$$Z_R << L_d << L_{pd}. \tag{147}$$

Considering the case of $a_0 = 0.5$, $\lambda_L = 0.8\mu$m, $n_0 = 10^{18}$cm$^{-3}$ and $w_0 = 33.5\mu$m, the corresponding lengths are $Z_R = 0.44$cm, $L_d = 3$cm and $L_{pd} = 11.7$cm. Taking the self-focusing effect into consideration, the electron energy gain is thus limited by dephasing.

In the relativistic case, the pump depletion length is found to be comparable to the dephasing length. A detailed discussion of the scaling law was given in Ref. [10]. If the electron acceleration is limited by the diffraction effect, $L_{acc} \approx \pi Z_R$, the energy gain is given by

$$W(\text{MeV}) = 740(\frac{\lambda_L}{\lambda_p}) \frac{1}{\sqrt{1 + a_0^2/2}} P(TW). \tag{148}$$

In the case limited by the dephasing length, $L_{acc} \approx L_d$, the energy gain is given by

$$W(\text{MeV}) = \frac{630 I(W/cm^2)}{n_0(cm^{-3})} \times \begin{cases} 1 & if \;\; a_0^2 << 1 \\ \frac{2}{\pi N_p} & if \;\; a_0^2 >> 1 \end{cases} \tag{149}$$

In the case limited by the pump depletion length, $L_{acc} \approx L_{pd}$, the energy gain is given by

$$W(\text{MeV}) = \begin{cases} \frac{3.4\times10^{21}}{\lambda_L^2(\mu m) n_0(cm^{-3})} & if \;\; a_0^2 << 1 \\ \frac{400 I(W/cm^2)}{n_0(cm^{-3})} & if \;\; a_0^2 >> 1 \end{cases} \tag{150}$$

It is important to note that the above scaling laws have been derived under the assumption of idealized conditions, which serve as a reference estimate. While there will inevitably be discrepancies between the theoretical predictions and the experimental measurements, the scaling laws provide a useful indication of the likely outcomes and a theoretical framework for optimizing the design of experiments.

### *3.4.5 Beam Loading*

In addition to the limit imposed by the acceleration length, the electron beam charge also exerts an influence on the LWFA, and thus has its own inherent limit. It should be noted that the wakefield can be induced not only by the laser pulse, but also by the injected electron beam. The net wakefield is the result of a superposition of the contributions from both the laser and the electron beam. Once the charge quantity of the electron beam is sufficiently large, the wakefield generated by the laser pulse is unable to provide further acceleration of the electrons. This

phenomenon is referred to as 'beam loading', i.e., the electrons inside the wakefield are saturated. Generally, beam loading has adverse impact on the beam quality and the acceleration efficiency. The energy spread under the beam loading condition is always broad. However, recent studies show that it is possible to modify the wakefield by controlling the beam loading [27]. The corresponding beam quality has been improved.

Here we have introduced the basic idea and some main mechanisms in LWFA. The subject of LWFA is currently undergoing rapid development. It is impossible to cover all the details and fresh results in this short lecture. To have a better understanding of LWFA and catch the latest progresses, it is necessary to refer to more papers.

# IV. Ion Acceleration

LWFA has high efficiency and long range acceleration since both the wakefield and the trapped electrons move with the velocities approaching to the speed of light. However, ions cannot catch up the fast plasma waves due to their heavier mass. The laser intensities available currently are not strong enough to kick the ions to high velocity over a short distance. Consequently, the acceleration of ions is primarily dependent on a static electric field with a substantial amplitude, such as the charge separation field in a high density target. The corresponding laser pulse should be sufficiently intense to interact with the solid density plasma. This section will provide a brief introduction for laser-plasma driven ion acceleration. More details of ion acceleration can be found in the nice review papers in Ref. [28–30].

### 4.1 Target Normal Sheath Acceleration (TNSA)

When the intense laser interact with the thin foil plasma, a large number of hot electrons will be produced. The hot electrons propagate in the laser direction and reach the rear side of the target. Consequently, a strong electrostatic field is generated normal to the rear surface of the target. The amplitude of the field is strong enough to accelerate ions in a short distance. Such the mechanism is known as target normal sheath acceleration (TNSA), which is first proposed in 2001 [31].

The schematic of TNSA is shown in Figure 23 from Ref. [30]. To model the sheath field, recall the MHD momentum equation for the ions and gives

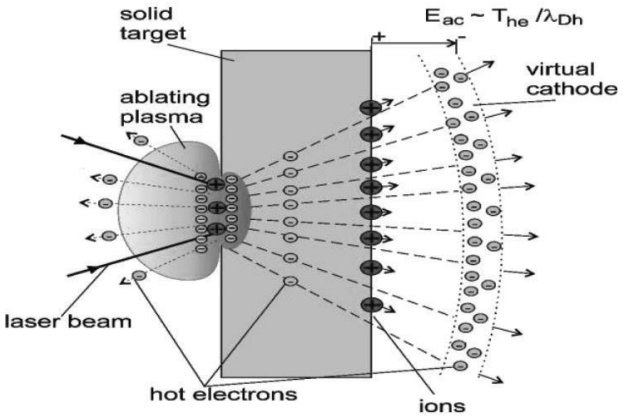


FIG. 23: The schematic of TNSA mechanism. Figure from Ref. [30].

$$\frac{\partial \mathbf{u}_i}{\partial t} + (\mathbf{u}_i \cdot \nabla)\mathbf{u}_i = \frac{Ze}{m_i}\mathbf{E}_s, \tag{151}$$

where the electrostatic field originates from the charge separation. Eq. (151) can be rewritten as

$$\frac{\partial \mathbf{u}_i}{\partial t} + (\mathbf{u}_i \cdot \nabla)\mathbf{u}_i = -\frac{c_s^2}{n_i}\nabla n_i, \tag{152}$$

where $c_s = \sqrt{Zk_BT_e/m_i}$ is the ion sound velocity. Define $\xi = x/t$ and operate the Eulerian transformation gives $n_i = N(\xi)$ and $u_i(x,t) = V(\xi)$. Then the MHD continuity equation and momentum equation become

$$\begin{cases} \frac{dN}{Nd\xi} = -\frac{V-\xi}{c_s} \\ \frac{dV}{d\xi} = -\frac{dN}{Nd\xi}(V-\xi). \end{cases} \tag{153}$$

Solving Eqs. (153) and returning back to the original coordinates gives the ion density and velocity expression

$$\begin{cases} n_i = n_0 \exp(-\frac{x}{c_s t} - 1) \\ u_i = c_s + x/t \end{cases} \tag{154}$$

The corresponding scenario of the isothermal plasma expansion can be seen in Figure 24 from Ref. [29]. The charge separation front locates at $x_f(t)$ and the rarefaction front at $-c_s t$. It should be noted that the expressions in Eqs. (154) only valid in the region of $-c_s t < x < x_f(t)$.

Based on Eqs. (154), the ion velocity is observed to increase infinitely. There must be a cutoff position for the thermal expansion. Considering the local density scale length equals to the local Debye length,

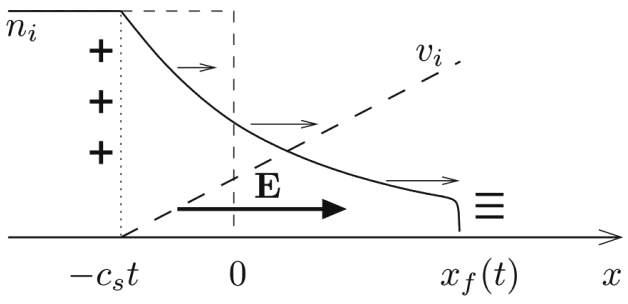


FIG. 24: Density and velocity distributions of the thermal expansion plasma. Figure from Ref. [29].

i.e. $c_s t = \lambda_D$, the charge separation front and the velocity are given as

$$\begin{cases} x_f = c_s t[2\ln(\omega_{pi}t) - 1] \\ u_f = 2c_s \ln(\omega_{pi}t) \end{cases} \tag{155}$$

where $\omega_{pi} = \sqrt{4\pi n_i Z^2 e^2/m_i}$ is the ion plasma frequency. The electric field at ion front is

$$E_f = \frac{2E_0}{\omega_{pi}t}, \tag{156}$$

where $E_0 = \sqrt{4\pi n_0 T_h}$ and $T_h$ is the hot electron temperature. Eqs. (154) also has a singularity at $t = 0$, which is solved by assuming only a single ion population and a single temperature electron at the initial condition [32]. The corresponding electric field and ion velocity can be expressed as

$$\begin{cases} E_x = 2E_0/\sqrt{2e + \omega_{pi}^2 t^2} \\ u_i = 2c_s \ln[\frac{\omega_{pi}t}{\sqrt{2e}} + (\frac{\omega_{pi}^2 t^2}{2e} + 1)^{1/2}]. \end{cases} \tag{157}$$

The sheath field strength and the accelerated ion energy are proportional to the hot electron temperature, which is then determined by the laser amplitude ($\sim \sqrt{I\lambda_L^2}$).

### 4.2 Radiation Pressure Acceleration (RPA)

Radiation Pressure Acceleration (RPA) was proposed in 2004 based on ultra-intense laser pulse [33]. The hydrodynamics of laser-plasma interactions are typically influenced by the thermal pressure and the radiation pressure (ponderomotive force). In the case of ultra-intense laser pulse, the radiation pressure dominates the laser-plasma interactions by directly pushing the target inwards. An electron layer are separated from the plasma ions and the so-called double layer structure is then formed. The large charge separation field accelerates ions along the longitudinal direction. This process is often called as 'hole-boring'. The schematic of RPA is shown in Figure 25.

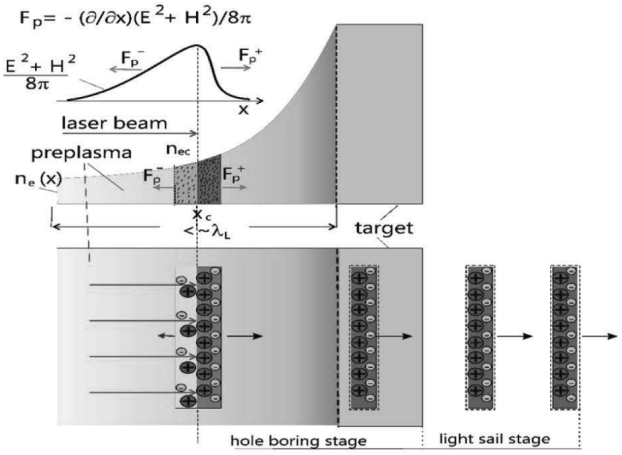


FIG. 25: The schematic of RPA mechanism. Figure from Ref. [30].

During the stage of hole-boring, both the energy and the charge quantity of the ion layer are increasing. Hole-boring terminates when the ion layer reaches at the rear surface of the target. After that, the both the electron and the ion layer will be accelerated by the radiation pressure in the free space. It is also called as a light-sail stage by imaging a sail pushed by the wind.

For a laser field incident into the target in the normal direction, the balance of the radiation pressure and the electrostatic pressure gives

$$\frac{E_s^2}{8\pi} = I\frac{(1+R-T)}{c}, \tag{158}$$

where R and T are the reflection and transmission coefficients of the target. Solving the Possion's equation of the double layer structure, the maximum energy gain of the ions can be expressed as

$$W_{max} = \frac{\xi^2}{2(1+\xi)} m_p c^2, \tag{159}$$

where $\xi = 2\pi\frac{Z}{A}\frac{m_e}{m_p}\frac{a_0^2\tau}{\zeta}$ and $\zeta = \pi\frac{n_e}{n_c}\frac{L}{\lambda_L}$. RPA normally requires that the laser intensity higher than $10^{21}\mathrm{W/cm}^2$. It is more efficient in the case of circularly polarized (CP) laser beams since the ponderomotive force of CP laser does not contain the high frequency component of $2\omega_L$. The interaction with a CP laser is therefore steady, due to the exclusion of time oscillation.

It should be noted that laser-driven ion acceleration is a rapidly developing research topic. There are many other mechanisms such as magnetic vortex acceleration (MVX) [34], Coulomb explosion (CE) [35], Break-out-afterburner (BOA) [36], shock wave acceleration (SWA) [37] in addition to the aforementioned TNSA and RPA. Figure 26 shows the main ion acceleration mechanisms with respect to the laser and plasma parameters [38]. Ion acceleration has important potential applications in heavy ion therapy, nuclear physics, fast ignition inertial confinement fusion and fundamental particle physics. We cannot cover all the regimes and the corresponding applications here. For the readers interested in this topic, more reviews can be found in the references of this section.

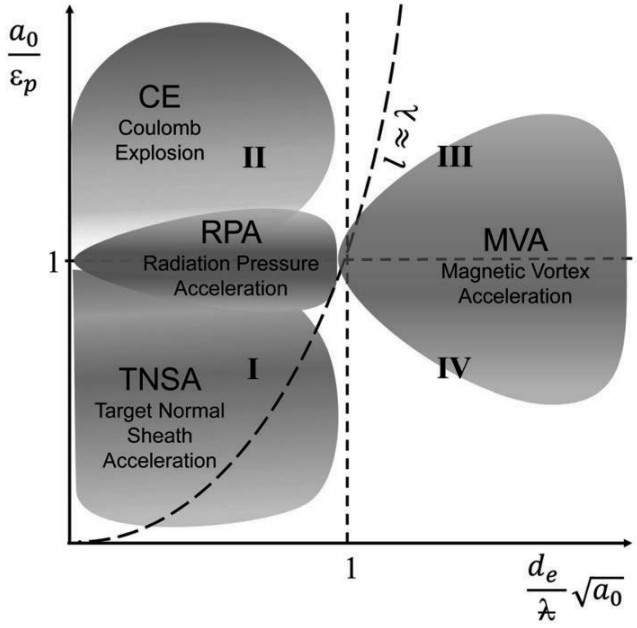


FIG. 26: Some basic laser ion acceleration mechanisms. Figure from Ref. [38]

## V. Kinetic Simulation

As mentioned in the previous sections, the laser-plasma interactions for charged particle acceleration are highly nonlinear. Only several cases with low laser intensity and underdense plasmas can be solved analytically. Actually not only in plasma physics, but in the vast majority of research areas dealing with complex systems, one has to resort to numerical methods and large computers to simulate the physical processes and obtain the detailed images. Numerical simulation has become the third type of physics research field after theoretical and experimental physics.

Concerning the plasma physics, there are mainly two kinds of simulation methods. One is the magnetohydrodynamics (MHD) approach based on the fluid theory where plasma is treated as the Single-fluid or Two-fluids models. The other one is the Particle-in-cell (PIC) approach based on the kinetic theory in which plasma is treated as a statistical sample of particles. MHD method has widely applications in ICF. However, specified to the topic of charged particle acceleration, PIC method has its unique advantages. PIC is implemented from first principles which significantly reduces the demanding to the equation of state. Unlike MHD simulations that rely on the system being in a Maxwell distribution, PIC method can resolve dynamical processes that deviate from the equilibrium states, which is necessary to describe the particle acceleration. There are many PIC codes available nowadays such as EPOCH [39], OSIRIS [40], SMILEI [41], VLPL [42], FBPIC [43], and so on. Although these well developed codes release the researchers from headache on writing their own code, it's still not a simple task to obtain the credible physical processes and images via simulation. The numerical errors induced by improper setup may cover the real interactions and present the misleading results. Excessive simulation precision, while not leading to the wrong results, will make the simulations and calculations extremely expensive. Therefore it is necessary to understand some basic algorithms of the PIC code even as a pure user.

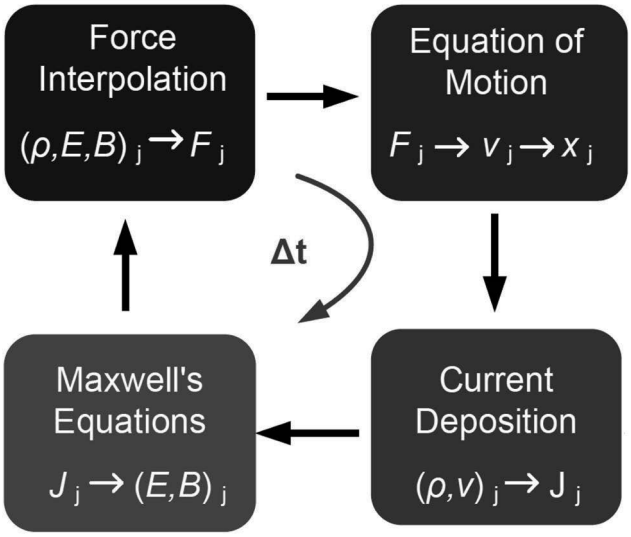


FIG. 27: Schematics of PIC code cycle.

Fig. 27 shows a typical PIC loop in one time-step, which is common for most of the PIC codes. Generally, PIC loop contains four steps. The first is the calculation of electromagnetic field onto the particles by interpolation of the fields. The second is the advancing of the particles by solving the equations of

motion. The third is the deposition of charge and current densities onto the mesh grids. The fourth step is to update the electromagnetic fields on the mesh grids by solving Maxwell's equations. These four steps complete the iteration within a predefined time-step, which should be carefully chosen depending on the physical problem under consideration. Each step in the loop contains some special algorithms to reach specific computational purposes, which include FDTD method, the particle pusher, field interpolation and current deposition. In this chapter, a brief introduction of these algorithms will be given. It should be noted that even with the algorithms, it takes a lot of effort to implement them in programming. For the pure user there is now a large amount of open source codes available for download, and the programming step may not seem necessary. However, reading the code in the context of the algorithms still helps the user to have a better understanding of the open source codes being used.

### 5.1 FDTD Solver for Maxwell's equations

The Finite-Difference Time-Domain (FDTD) method was first formulated by Yee [44] and has been widely applied in many PIC codes as the standard Maxwell-solver. All the field components are located on the grids called as 'Yee lattice'. Then the time-dependent Maxwell's equations are discretized and are further solved either in a central difference method or in a leapfrog manner.

The normalized Maxwell's equation can be written as

$$\begin{cases} \frac{\partial \mathbf{E}}{\partial t} = \nabla \times \mathbf{B} - \mathbf{J} \\ \frac{\partial \mathbf{B}}{\partial t} = -\nabla \times \mathbf{E}. \end{cases} \tag{160}$$

The Gauss's law for electric and magnetic field are self-consistent under certain conditions. Consider $\nabla \cdot \partial_t \mathbf{B} = -\nabla \cdot (\nabla \times \mathbf{E}) = 0$, which implies $\partial_t (\nabla \cdot \mathbf{B}) = 0$. Therefore, if $\nabla \cdot \mathbf{B} = 0$ is initially satisfied, it will always be satisfied. Recall the continuity equation similar to Eq. (42),

$$\frac{\partial \rho}{\partial t} + \nabla \cdot \mathbf{J} = 0. \tag{161}$$

Compare with the first equation in Eqs. (160), it gives that $\nabla \cdot \mathbf{E} = \rho$. Therefore, under the condition of charge conservation, the Gauss's law for electric field is always satisfied. Thus only Maxwell's equations in Eqs. (160) are required for the update of the electromagnetic field in time. The vector equations can be expressed in the scalar form with the following components,

$$\begin{cases} \partial_t E_x = (\partial_y B_z - \partial_z B_y) - J_x \\ \partial_t E_y = (\partial_z B_x - \partial_x B_z) - J_y \\ \partial_t E_z = (\partial_x B_y - \partial_y B_x) - J_z \\ \partial_t B_x = -(\partial_y E_z - \partial_z E_y) \\ \partial_t B_y = -(\partial_z E_x - \partial_x E_z) \\ \partial_t B_z = -(\partial_x E_y - \partial_y E_x) \end{cases} \tag{162}$$

The distributions of the electric and magnetic field on the grids are shown in Figure 28. Noted that **B** and **E** are half mesh separated while **J** and **E** are located in the same position on the mesh.

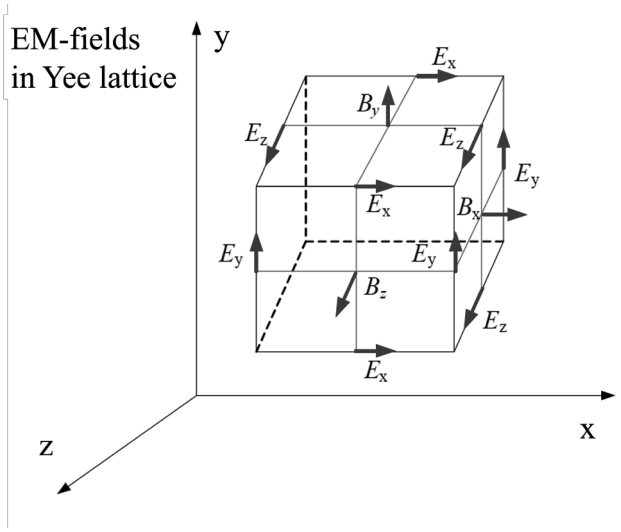


FIG. 28: The electromagnetic fields in the Yee lattice.

Thus the curl operation can be calculated as follows:

$$\begin{aligned} &\frac{(E_x)^{n+1}_{i+1/2,j,k} - (E_x)^{n}_{i+1/2,j,k}}{\Delta t} = -(J_x)^{n+1/2}_{i+1/2,j,k} \\ &+ \frac{(B_z)^{n+1/2}_{i+1/2,j+1/2,k} - (B_z)^{n+1/2}_{i+1/2,j-1/2,k}}{\Delta y} \\ &- \frac{(B_y)^{n+1/2}_{i+1/2,j,k+1/2} - (B_y)^{n+1/2}_{i+1/2,j,k-1/2}}{\Delta z}, \end{aligned} \tag{163}$$

$$\begin{aligned} &\frac{(B_x)^{n+3/2}_{i,j+1/2,k+1/2} - (B_x)^{n+1/2}_{i,j+1/2,k+1/2}}{\Delta t} = \\ &\frac{(E_y)^{n+1}_{i,j+1/2,k+1} - (E_y)^{n+1}_{i,j+1/2,k}}{\Delta z} \\ &- \frac{(E_z)^{n+1}_{i,j+1,k+1/2} - (E_z)^{n+1}_{i+1/2,j,k+1/2}}{\Delta y}. \end{aligned} \tag{164}$$

To be simplified, here only the components of $E_x$ and $B_x$ are presented. The others can be easily implemented by changing the footnotes in order.

One of the most important constraints in PIC is the so-called Courant-Friedrichs-Lewy (CFL) condition [45]. The principle of the condition is that the wave traveling across a discrete spatial grid should not propagate more than one cell per time step. Therefore it restricts the time step parameter $\Delta t$ in PIC by

$$c\Delta t \leq \frac{1}{\sqrt{1/\Delta x^2 + 1/\Delta y^2 + 1/\Delta z^2}}, \tag{165}$$

which is the valid for the 3D case. CFL condition is also called as the numerical stability condition related to the numerical dispersion. Actually CFL condition is not specified to PIC code. In many PDE (partial differential equations) solver with explicit time-marching method, such the condition must be satisfied to avoid incorrect or unstable results.

The phase velocity of the numerical electromagnetic fields with respect to the mesh resolution is shown in Figure 29 from Ref. [46]. FDTD solver is subject to numerical dispersion as the wave velocity is found to depend on its wavenumber and propagation orientation. For a typical simulation of normal incident, a sufficient high resolution is necessary.

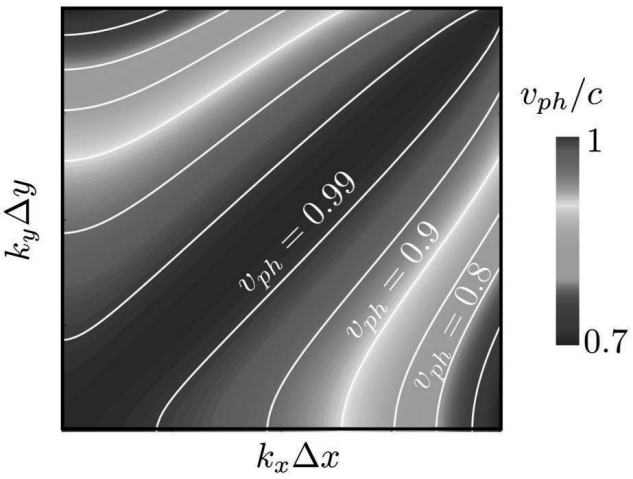


FIG. 29: Phase velocity of EM fields with respect to the numerical resolution. Figure from Ref. [46]

### 5.2 Particle-pusher for equations of motion

The particle-pusher advances the particles information in time and space by solving the Lorentz-Newton equation. This allows the density and current distribution to be updated for further advancement of Maxwell's equations. In relativistic condition, the dimensionless Lorentz-Newton equation can be written as

$$\frac{d(\gamma m_e \mathbf{v})}{dt} = -e(\mathbf{E} + \mathbf{v} \times \mathbf{B}). \tag{166}$$

To update the position, one need the definition of the velocity,

$$\frac{d\mathbf{x}}{dt} = \mathbf{v}. \tag{167}$$

Discretizing the above equations gives,

$$\begin{cases} \mathbf{u} = \gamma \mathbf{v} \\ \frac{\mathbf{u}^{n+1/2} - \mathbf{u}^{n-1/2}}{\Delta t} = \frac{-e}{m_e}[\mathbf{E}^n + \frac{\mathbf{u}^{n+1/2} + \mathbf{u}^{n-1/2}}{2\gamma^n} \times \mathbf{B}^n] \\ \frac{\mathbf{x}^{n+1} - \mathbf{x}^n}{\Delta t} = \frac{\mathbf{u}^{n+1/2}}{\gamma^{n+1/2}} \end{cases} \tag{168}$$

where $\mathbf{u}$ is the commonly used normalized velocity and $\gamma^n = (\gamma^{n+1/2} + \gamma^{n-1/2})/2$.

In a typical PIC simulation, the number of particles reaches more than $10^9$. The particle-pusher is the most time consuming part in the PIC loops and it is easy to introduce the error of numerical heating. The method for the particle-pusher should be handled carefully. In the modern PIC codes, the Boris-Pusher algorithm [47] is the most well-established and commonly used method for solving the Lorentz-Newton equations due to its excellent properties such as high stability, energy conservation, avoidance of cross-product computations, and time reversibility. By observing Eqs. (168), it can be seen that the electric field component is easily calculated by the leap-frog method, as used in FDTD. However, the curl operation on the magnetic field is difficult to solve since it contains the term of $\mathbf{u}^{n+1/2}$ on both sides of the equation. The basic idea of the Boris-Pusher is to separate the acceleration phase contributed by the electric field and the rotation phase contributed by the magnetic field in Eq. (166). First use the following substitution for the normalized velocity:

$$\begin{cases} \mathbf{u}^{n-1/2} = \mathbf{u}^- - \frac{-e\mathbf{E}^n}{m_e}\frac{\Delta t}{2} \\ \mathbf{u}^{n+1/2} = \mathbf{u}^+ + \frac{-e\mathbf{E}^n}{m_e}\frac{\Delta t}{2} \end{cases} \tag{169}$$

Plugging Eqs. (169) back to Eqs. (168), the electric field term will be eliminated and gives,

$$\frac{\mathbf{u}^+ - \mathbf{u}^-}{\Delta t} = \frac{-e}{2m_e\gamma^n}(\mathbf{u}^+ + \mathbf{u}^-) \times \mathbf{B}^n. \tag{170}$$

Noted that the term $\mathbf{u}^-$ is known since $\mathbf{u}^- = \mathbf{u}^{n-1/2} - e\mathbf{E}^n\Delta t/2m_e$. Building a new vector $\mathbf{b}$ to substitute the magnetic field as:

$$\mathbf{b} = \frac{-e\mathbf{B}^n}{m_e\gamma^n}\frac{\Delta t}{2}. \tag{171}$$

A new velocity vector can be expressed as

$$\mathbf{u}^* = \mathbf{u}^- + \mathbf{u}^- \times \mathbf{b}. \tag{172}$$

Since both $\mathbf{u}^-$ and $\mathbf{b}$ are known, the velocity of $\mathbf{u}^*$ can also be computed. Building another vector parallel to $\mathbf{b}$ as:

$$\mathbf{s} = \frac{2\mathbf{b}}{1+|\mathbf{b}|^2}. \tag{173}$$

The geometrical relation among $\mathbf{u}^*$, $\mathbf{s}$, and $\mathbf{u}^-$ gives

$$\mathbf{u}^+ = \mathbf{u}^- + \mathbf{u}^* \times \mathbf{s}. \tag{174}$$

Thus it reaches our final goal $\mathbf{u}^{n+1/2}$ according to the second equation in Eqs. (169).

### 5.3 Grid field interpolation

One problem that remains in the particle-pusher is how to determine the force acting on the particles, i.e. the electric and magnetic field strength at the particle position. As mentioned above, the field information in the PIC code is only distributed on the grids. However, the particles can be located anywhere in the simulation box. It is necessary to do the interpolation of the grid fields to the particles positions. Similarly, when we consider the charge and current on the grids contributed by the particles, the interpolation should be operated again from the particle positions to the grids.

The interpolation is based on the so-called shape function of the particles, which controls the smoothness of the solution. In PIC code, one of the key ideas is to express the distribution function via a sum of the macroparticles as,

$$f(t,\mathbf{x},\mathbf{p}) = \sum_{p=1}^{N} w_p S(\mathbf{x}-\mathbf{x}_p(t))\delta(\mathbf{p}-\mathbf{p}_p(t)), \tag{175}$$

where $N$ is the total number of the macroparticles, $w_p$ is the weight representing their ratio to the real particles, $S(x)$ is the spatial shape function. It should be particularly noted that the macroparticles in PIC are not the mass points. They have the sizes expressed by the spatial shape function. The delta function $\delta(\mathbf{p}-\mathbf{p}_p(t))$ guarantees that each particle has one velocity in order to avoid the expansion in phase space.

In the pioneering PIC codes, the shape function also took the form of a delta function. In contrast, the shape functions in the modern PIC codes are mainly the b-splines with different orders. The zeroth order b-spline is a top hat function as

$$S(x) = \begin{cases} 1 & if \ \ |x| \le \Delta x/2 \\ 0 & otherwise \end{cases} \tag{176}$$

which is also known as the nearest-grid-point (NGP) function. In this case, each electron is like a rod with same length $\Delta x$ between the grid points, which contributes charge density $e/\Delta x$. The first order b-spline is a triangle function as

$$S(x) = \begin{cases} 1-|x|/\Delta x & if \ \ |x| \le \Delta x \\ 0 & otherwise \end{cases} \tag{177}$$

Such the continuous linear interpolation is called as the cloud-in-cell (CIC). The charge contributed by the electron linearly decreases from $e/\Delta x$ to 0 in the distance of one cell. In many PIC codes, the first order shape is set as default. The form of the second order becomes more complicate as:

$$S(x) = \begin{cases} (\frac{x}{\Delta x}+1.5)^2/2 & if \ \ -1.5\Delta x \le x \le -0.5\Delta x \\ [-2(\frac{x}{\Delta x})^2+1.5]/2 & if \ \ x| \le \Delta x/2 \\ [3-(\frac{x}{\Delta x}+1.5)]^2/2 & if \ \ 0.5\Delta x \le x \le 1.5\Delta x \\ 0 \qquad otherwise \end{cases} \tag{178}$$

The first three b-splines of the spatial shape functions are shown in Figure 30. The higher order shape function results in a higher resolution with the cost of heavier computing. Therefore, a sufficient order for a certain physical model should be carefully considered to balance the efficiency and accuracy.

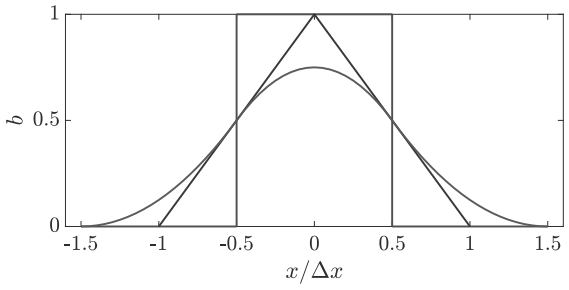


FIG. 30: The first three orders of the spatial shape functions.

Once the shape function has been determined, the electric and magnetic fields calculated at the discrete grids can be assigned to the particle positions as,

$$\begin{cases} \mathbf{E}_p^n = \sum_{ijk} \mathbf{E}_{ijk}^n S(\mathbf{x}_{ijk}-\mathbf{x}_p^n) \\ \mathbf{B}_p^n = \sum_{ijk} \mathbf{B}_{ijk}^n S(\mathbf{x}_{ijk}-\mathbf{x}_p^n) \end{cases} \tag{179}$$

### 5.4 Current deposition

After updating the velocities and positions of the particles by Eq. (174) and Eqs. (169), it is possible to calculate the charge density $\rho$ and current density $\mathbf{J}$ on the grid. Under the condition of charge conservation, J. Villasenor and O. Buneman [48] provided a method for calculating the current density based on the first-order shape function (CIC). However, the form of the calculation is complicated due to the consideration of various boundary conditions. Later, T. Esirkepov [49] proposed a unified form of current density calculation with an arbitrary order shape function, which can be implemented directly in the PIC code. The current density contributed by a particle is computed as:

$$\begin{cases} (J_x)^{n+1/2}_{i+1/2,j,k} - (J_x)^{n+1/2}_{i-1/2,j,k} = -q_s \frac{\Delta x}{\Delta t}(S_x)^{n+1/2}_{i,j,k} \\ (J_y)^{n+1/2}_{i,j+1/2,k} - (J_y)^{n+1/2}_{i,j-1/2,k} = -q_s \frac{\Delta y}{\Delta t}(S_y)^{n+1/2}_{i,j,k} \\ (J_z)^{n+1/2}_{i,j,k+1/2} - (J_z)^{n+1/2}_{i,j,k-1/2} = -q_s \frac{\Delta z}{\Delta t}(S_z)^{n+1/2}_{i,j,k} \end{cases} \tag{180}$$

The shape functions are recalled again for the current deposition. The particle shape function appear in two places in PIC. First is when the EM fields are interpolated to the position of the particle as we mentioned above. Second is here when the current is updated and properties of the particle are copied onto the grids.

So far, the main loops and algorithms of the PIC method have been discussed. Most of the popular codes are based on the above frames and the fundamental laser-plasma interactions can be well calculated. Modern PIC codes may also include other physical packages such as Coulomb collisions, atomic reaction, radiation, and QED effects. The discussion of these specific tools is beyond the scope of this lecture. Although the principles are not difficult, it requires careful design and setup to launch a proper simulation for a specific physical model. The PIC code is easily affected by numerical dispersion, self-heating, numerical Cherenkov instability and other numerical instabilities. Experience and a better understanding of the physical processes are necessary to perform reliable simulations.

## VI. Summary

This mini-review presents an overview of the fundamental theories of laser-plasma interactions and charged particle acceleration principles. A comprehensive relation between the laser and plasma parameters are provided via formulas for obtaining the practical scaling laws. The numerical tools of kinetic simulation are briefly introduced for beginners and pure users. Many relevant articles are not referenced here due to the limitation constraints. Readers interested in this topic may find more detailed literature here [2, 3, 10, 29, 50, 51].

## Acknowledgments

This work was funded by the JST-MIRAI program grant no. JPMJMI17A1. We are grateful to the technical teams of Spring-8 Center for their support of the Laser Acceleration Platform. We acknowledge the use of the supercomputer facility of the Cybermedia Centre at Osaka University.

[1] F. F. Chen, *Introduction to Plasma Physics* (Springer New York, 1974).
[2] P. Gibbon, *Short Pulse Laser Interactions with Matter* (Imperial College Press, 2005).
[3] V. Malka, Phys. Plasmas **19**, 055501 (2012).
[4] T. Tajima, and J. Dawson, Phys. Rev. Lett. **43**, 267 (1979).
[5] W. P. Leemans, et al., Phys. Rev. Lett. **113**, 245002 (2014).
[6] A. J. Gonsalves, et al., Phys. Rev. Lett. **122**, 084801 (2019).
[7] T. Coffey, et al., Phys. Fluids **14**, 1402 (1971).
[8] C. Schroeder, et al., Phys. Rev. E **72**, 055401 (2005).
[9] S. V. Bulanov, et al., Phys. Rev. Lett. **74**, 710 (1995).
[10] E. Esarey, et al., Rev. Mod. Phys. **81**, 1229 (2009).
[11] S. Steinke, et al., Nature **530**, 190 (2016).
[12] E. Adli, et al., Nature **561**, 363 (2018).
[13] X. Stragier, et al., SPIE **8079**, 80790W (2011).
[14] D. Umstadter, et al., Phys. Rev. Lett. **76**, 2073 (1996).
[15] E. Esarey, et al., Phys. Rev. Lett. **79**, 2682 (1997).
[16] M. Chen, et al., J. App. Phys. **99**, 056109 (2006).
[17] A. Pak, et al., Phys. Rev. Lett. **104**, 025003 (2010).
[18] L. Yu, et al., Phys. Rev. Lett. **112**, 025001 (2014).
[19] H. Suk, et al., Phys. Rev. Lett. **86**, 1111 (2001).
[20] Z. Lei, et al., High Power Laser Sci. Eng. **11**, e91 (2023).
[21] Z. Lei, et al., Rev. Sci. Instrum. **95**, 015111 (2024).
[22] A. Butler, et al., Phys. Rev. Lett. **89**, 185003 (2002).
[23] K. Nakamura, et al., Phys. Plasmas **14**, 056708 (2007).
[24] A. Gonsalves, et al., Phys. Rev. Lett. **122**, 084801 (2019).
[25] E. Esarey, et al., Proceedings of the Advanced Accelerator Concepts Workshop **737**, 578 (2004).
[26] B. Shadwick, et al., Phys. Plasmas **16**, 056704 (2009).
[27] M. Tzoufras, et al., Phys. Plasmas **16**, 056705 (2009).
[28] H. Daido, et al., Rep. Prog. Phys. **75**, 056401 (2012).
[29] A. Macchi, et al., Rev. Mod. Phys. **85**, 751 (2013).
[30] J Badziak, J. Phys.: Conf. Ser. **959**, 012001 (2018).
[31] S. Wilks, et al., Phys. Plasmas **8**, 542 (2001).
[32] A. Lifschitz, et al., New J. Phys. **16**, 033031 (2014).
[33] T. Z. Esirkepov, et al., Phys. Rev. Lett. **92**, 175003

(2004).
[34] S. V. Bulanov, et al., Phys. Rev. Lett. **98**, 049503 (2007).
[35] S. V. Bulanov, et al., Phys. Lett. A **299**, 240 (2002).
[36] B. Albright, et al., Phys. Plasmas **14**, 094502 (2007).
[37] D. Haberberger, et al., Nat. Phys. **8**, 95 (2012).
[38] S. S. Bulanov, et al., Phys. Plasmas **23**, 056703 (2016).
[39] T. Arber, et al., Plasma Phys. Control. Fusion **57**, 113001 (2015).
[40] R. G. Hemker, et al., IEEE Particle Accelerator Conference **5**, 3672 (1999).
[41] J. Derouillat, et al., Comput. Phys. Commun. **222**, 351 (2018).
[42] A. Pukhov, J. Plasma Phys. **61**, 425 (1999).
[43] R. Lehe, et al., Comput. Phys. Commun. **203**, 66 (2016).
[44] K. Yee, IEEE Trans. Antennas Propag. **14**, 302 (1966).
[45] R. Courant, K. Friedrichs, and H. Lewy, Mathematische Annalen **100**, 32 (1928).
[46] R. Nuter, et al., Eur. Phys. J. D **68**, 177 (2014).
[47] J. Boris, and R. Shanny, Fourth Conference on Numerical Simulation of Plasmas: Proceedings, **2**, 3 (1972).
[48] J. Villasenor, and O. Buneman, Comput. Phys. Commun. **69**, 306 (1992).
[49] T. Z. Esirkepov, Comput. Phys. Commun. **135**, 144 (2001).
[50] S. V. Bulanov, et al., J. Plasma Phys. **82**, 905820308 (2016).
[51] T. Tajima, et al., Rev. Mod. Plasma Phys. **4**, 7 (2020).